

RICE UNIVERSITY

Plasmonic Properties of Metallic Nanostructures

by

Tae-Ho Park

A THESIS SUBMITTED
IN PARTIAL FULFILLMENT OF THE
REQUIREMENTS FOR THE DEGREE
DOCTOR OF PHILOSOPHY

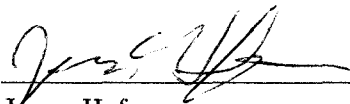
APPROVED, THESIS COMMITTEE:



Peter Nordlander, Chair
Professor of Physics and Astronomy;
Professor of Electrical and Computer
Engineering



Naomi Halas
Stanley C. Moore Professor of Electrical
and Computer Engineering; Professor of
Chemistry



Jason Hafner
Associate Professor of Physics and
Astronomy; Associate Professor of
Chemistry

Houston, Texas

May, 2009

UMI Number: 3421176

All rights reserved

INFORMATION TO ALL USERS

The quality of this reproduction is dependent upon the quality of the copy submitted.

In the unlikely event that the author did not send a complete manuscript and there are missing pages, these will be noted. Also, if material had to be removed, a note will indicate the deletion.



UMI 3421176

Copyright 2010 by ProQuest LLC.

All rights reserved. This edition of the work is protected against unauthorized copying under Title 17, United States Code.



ProQuest LLC
789 East Eisenhower Parkway
P.O. Box 1346
Ann Arbor, MI 48106-1346

ABSTRACT

Plasmonic Properties of Metallic Nanostructures

by

Tae-Ho Park

Based on the plasmon hybridization theory, this thesis provides physical understanding of the plasmonic nature of metallic nanostructures. Metallic films and nanoshell particles exhibit bonding and antibonding plasmon resonances formed by hybridization of plasmon resonances associated with the two surfaces confining the metal. For both structures the lower energy bonding plasmon resonance is characterized by a symmetric alignment of the charge densities. This thesis presents a physically intuitive explanation for why the repulsive symmetric charge alignment results in a low energy bonding plasmon. It also shows that the plasmon dispersion for a planar thin film can be obtained from the plasmon resonances of a metallic nanoshell in the limit of infinite radius.

After clarifying the nature of plasmon modes of thin metal films, the optical properties of an individual nanohole in a thin metallic film are examined theoretically and experimentally. Subwavelength holes, one of the most important structures in

nanophotonics, give rise to extraordinary transmission when patterned in arrays. The individual holes provided a site for excitation of the underlying thin film surface plasmons. It is shown that both hole diameter and film thickness determine the energy of the optical resonance. I also show that the hole plasmon resonance (HPR) depends strongly on the polarization of the incident light due to the optical coupling between antibonding film plasmon modes and perpendicularly polarized light to the film surface.

The hybridization scheme is extended to the coherent coupling between the localized plasmons of a nanoshell and the excitons of J-aggregate molecules adsorbed on the metallic nanoparticle surface. Tuning the nanoshell plasmon resonant energies across the exciton energy of the J-aggregate obtains hybridized energies for plasmon-exciton coupling. The coupling strength depends on the specific plasmon mode of the nanoshell coupled to the exciton mode of the J-aggregate. Experimental data of optical extinction spectra is reproduced by using Mie theory, and the plasmon-exciton coupling of nanoshell/J-aggregate complexes systems can be quantitatively as well as qualitatively understood based on Gans theory.

The plasmon hybridization theory can be also applied to various shapes of nanoparticles using particular coordinate systems. This thesis investigate the optical properties of metallic toroidal nanoparticles using the plasmon hybridization theory. For incident light polarized in the plane of the torus, a low energy dipolar plasmon reso-

nance and a high energy resonance contributed by several higher order torus modes appear in the optical spectra. The low energy mode is highly tunable with the aspect ratio in terms of two characteristic radii of tori. For perpendicular polarization, the plasmon resonance is weakly dependent on the aspect ratio because the excited higher order torus modes are closely spaced. Optical spectra calculated by plasmon hybridization method show excellent agreement with numerical finite difference time domain calculation results.

Acknowledgments

I am deeply grateful to my advisor, Prof. Peter Nordlander for his guidance and instruction. I have respected his great passion for physics, and diligence. His elegant and clear descriptions to explain physical phenomena in simple ways have been constantly inspiring my research. I am also deeply thankful to Prof. Naomi Halas for encouragement of my research with a lot of fruitful discussions through collaboration and weekly LANP meeting. I would like to thank my previous and current group members, Dr. Daniel Brandl, Dr. Fei Le, Mr. Yanpeng Wu, Mr. Feng Hao, Mr. Britan Willingham, Mr. Tamer Ali, Mr. Jorge Zuloga, Mr. Kui Bao, Mr. Heidar Khakestar, and Dr. Chizuko Dutta, for their invaluable discussions. I would like to thank my collaborators in research, Mr. Nche Tumassang Fofang, Mr. Nikolay Mirin, Mr. Britt Lassiter, Dr. Joong-Wook Lee, and Prof. Daniel Mittleman for their contributions and enlightenment to my research. I would like to thank Prof. Naomi Halas, Prof. Jason Hafner for taking time off their busy schedules to participate in my thesis defense. I also would like to thank the Laboratory for Nanophotonics (LANP), a great platform for my exposure to latest publications and discussions with experimentalists. I would like to thank my family, especially my parents and my lovely wife Su-Jung who has been constantly supporting me.

Contents

Abstract	ii
Acknowledgments	v
List of Figures	ix
1 Introduction	1
2 Bonding and antibonding metallic film and nanoshell plasmons	8
2.1 Introduction	8
2.2 Bonding and Antibonding Plasmon Modes	9
2.3 Film Plasmons	13
2.4 Nanoshell Plasmons	16
2.5 Connection between Nanoshell and Film Plasmons	18
2.6 Dielectric and Electrodynamic Effects on Film Plasmons	20
2.7 Conclusion	25
3 Optical Properties of a Subwavelength Hole in a Thin Metallic Film	27
3.1 Introduction	27
3.2 Theory	30
3.3 Experiment	35
3.4 Results and Discussion	36

3.4.1	Hole Plasmon Resonance for a Nanosized Hole	36
3.4.2	Polarization Dependency	47
3.5	Conclusion	52
4	Plasmon-Exciton Coupling in Nanoshell/J-Aggregate Complexes	54
4.1	Introduction	54
4.2	Theory	55
4.3	Experiment	61
4.4	Results and Discussion	66
4.5	Conclusion	71
5	Plasmonic Properties of a Metallic Torus	73
5.1	Introduction	73
5.2	Theory	75
5.2.1	Plasmonic structure	76
5.2.2	Optical absorption	84
5.3	Results	86
5.3.1	Plasmonic structure	87
5.3.2	Optical absorption	91
5.3.3	Field enhancements and retardation effects	95
5.4	Discussion and Conclusion	96

viii

6 Conclusions

98

References

101

List of Figures

2.1	Mie calculations of the extinction spectrum, electric field enhancements, and charge density amplitudes for a nanoshell of geometry (20,25) nm.	10
2.2	Film plasmon dispersion, electric field profiles, and schematic surface charge density distribution for the bonding and antibonding film plasmon.	11
2.3	Illustration of the primary and secondary charge density distribution induced by the primitive plasmon modes for a film.	14
2.4	Illustration of the primary and secondary charge density distribution induced by a primitive dipolar plasmon modes for a nanoshell.	16
2.5	Illustration of the relation between the multipolar index l of a nanoshell plasmon and the wavevector k of a film plasmon.	19
2.6	Dispersion relations of film plasmons with realistic dielectric constants.	22
2.7	Imaginary part of the SPP wavevector as a function of the plasmon energy.	25
3.1	Schematic description of geometrical structure for the nanohole/film system.	30
3.2	Dipolar optical absorption spectra of the hole/film system calculated by the plasmon hybridization method.	37

3.3	Charge configuration for Bonding and antibonding film plasmon modes and the mechanism by which a nanohole allows coupling of light to these modes.	39
3.4	Dispersion relations calculated using Maxwell equations for a nanohole in a thin metal film, Skin depth of Au as a function of wavelength, and hole plasmon resonance comparison between retarded and electrostatic calculations.	41
3.5	Experimental measurement of optical scattering for different hole/film systems.	46
3.6	Dipolar optical absorption spectra of the hole/film system calculated by the plasmon hybridization method parallel and perpendicular polarization of incident light, and description for optimal coupling between bonding (antibonding) film plasmon modes and parallel (perpendicular) polarization light.	49
3.7	Comparison between theoretical expectation and experimental measurement of hole plasmon resonance.	51
4.1	Schematic description of gold nanoshell/J-aggregate complex.	57
4.2	Extinction spectra of J-aggregates, nanoshells, and nanoshell/J-aggregate complex.	63

4.3	SERS and normal Raman spectra of 2,2'-dimethyl-8-phenyl-5,6,5',6',- dibenzothiacarbocyanine chloride.	65
4.4	Experimental and Theoretical extinction spectra for dipolar plasmon modes of nanoshells and nanoshell/J-aggregate complexes, and disper- sion curves.	69
4.5	Experimental and Theoretical extinction spectra for quadrupolar plas- mon modes of nanoshells and nanoshell/J-aggregate complexes, and dispersion curves.	70
4.6	Onset of splitting in plasmon/J-aggregate complex as a function of dye concentration in media.	72
5.1	A schematic diagram of a torus and the toroidal angular coordinates.	77
5.2	Schematic illustration of the top and side views of the surface charge distribution.	81
5.3	Dispersion relation : The hybridized $\mu = 1$ cosine plasmon energy levels of a metallic torus as a function of the aspect ratio X	88
5.4	Plasmon hybridization in a torus for parallel polarization, i.e., $\mu = 1$ cosine modes.	89
5.5	Absorption cross sections for light of parallel polarization incident on a torus of aspect ratio $X=0.2$ (a) and $X=0.8$ (b) calculated using PH and FDTD.	92

5.6	Absorption cross sections for perpendicular polarization calculated using PH and FDTD for a torus of $X=0.5$	93
5.7	Effect of phase retardation on the tunable parallel torus mode.	94
5.8	Electric field enhancement of a toroid with an aspect ratio $X=0.5$ for the wavelength of the incident light is 811 nm.	95

Chapter 1

Introduction

The optical property of metallic nanostructures is a subject of considerable fundamental and technological importance. The excitation spectrum of a metallic nanostructure or sub-wavelength structure is determined by its surface plasmon resonances, which are collective oscillations of the conduction electrons. The energies of plasmon resonances can depend strongly on shape and composition of the nanostructure. Examples of highly tunable plasmonic nanoparticles are metallic nanoshells[1, 2] and nanorods[3, 4].

The tunability of the plasmon resonances of metallic nanoparticles can be exploited to position the optical resonances at specific wavelength regions of interest and has led to a wide range of applications across many disciplines in science and engineering. The strong local electro-magnetic field enhancement accompanied with the surface plasmon resonances has been also used to manipulate light-matter interactions, and metallic nanostructures on the sub-wavelength scale are widely used in Surface Enhanced Raman Spectroscopy (SERS) and Surface Enhanced Infrared Absorption (SEIRA). In addition to their fundamental importance, plasmonic nanostructures are receiving a great deal of attention for their potential applications in areas such as subwavelength waveguiding[5, 6], optical nanoantennas[7, 8], photovoltaic

technology for efficient light coupling into solar cells[9, 10], metamaterials[11, 12], chemical and biological sensing[13, 14], and biomedical applications[15].

The development of novel synthesis or lithography methods for nano-fabrication and nano-characterization techniques such as dark field and near-field optical microscopy make single nanostructure and sub-wavelength resolution measurements possible. Furthermore, the development of theoretical and numerical approaches such as Plasmon Hybridization (PH) theory, Finite Difference Time Domain (FDTD) method, Finite Element Method (FEM), Discrete Dipole Approximation (DDA), and Boundary Element Method (BEM) help for the understanding of their optical properties. Therefore, all these theoretical and experimental developments are making the field of anophotonics an area of intense current interest.

Based on the PH theory in this thesis, I clarify the optical and plasmonic properties of various metallic nanostructures such as nanoshells, thin films, individual sub-wavelength holes in thin metal film, nanoshell/J-aggregate complexes, and toroidal nanoparticles. The theoretical results are compared with experimental measurements and numerical calculations such as Mie theory for the system with spherical symmetry, and FDTD simulations.

The PH method was first invented to explain the behavior of gold nanoshell plasmons[1, 16]. In the PH theory, conduction electrons of metals are regarded as irrotational, incompressible fluids confined to a uniform positive background. The

primitive plasmons arise at each surface of a metallic nanostructures due to deformation of the fluid. The kinetic energy associated with the plasmons is balanced by a potential energy arising from the electrostatic interaction of the surface charges. Plasmons interact electrostatically with those from other surfaces in terms of instantaneous Coulomb potential. The PH method has been applied to several different types of nanostructures such as nanoparticle/surface[17], multi-particle[18, 19], nanoparticle/film[20], nanoparticle/wire[21] systems and successfully explained the shift of plasmon resonance in terms of coupling among different plasmon modes in analogy with molecular orbital theory.

Surface plasmon modes in metallic thin films and nanoshells may be viewed as arising from bonding and antibonding plasmon resonances formed by hybridization of primitive plasmons associated with the two surfaces confining the metal. In Chapter 2, I discuss the nature of the bonding and antibonding metallic film and nanoshell plasmons as a cornerstone of PH theory. Because conceptually symmetric and antisymmetric surface plasmon modes in thin metallic film have not been clearly defined, the unclear definition may lead to misunderstanding of the film plasmon modes[22, 23, 24]. The lower energy bonding plasmon mode is a symmetric alignment of the primitive plasmon modes associated with the two surfaces, while the higher energy antibonding mode has an antisymmetric alignment. This alignment of surface charges is counterintuitive since one would expect the Coulomb repulsion to be lower for an antisymmetric

alignment. I will also show that the plasmon dispersion for a planar thin film can be obtained from the plasmon resonances of a metallic nanoshell in the limit of infinite radius.

After clarifying the bonding and antibonding plasmon modes in thin metallic film in Chapter 2, I will discuss the optical properties of a subwavelength hole in a thin metallic film in Chapter 3. Theoretical studies on the diffraction of light through subwavelength holes in conducting screens began a half century ago with studies by Bethe and Bouwkamp[25, 26]. However, the nanosized aperture or nanohole in a thin metal film has received particular attention since the discovery of the extraordinary optical transmission (EOT) phenomenon in nanohole arrays [27]. Near-field optical experiments and modern numerical techniques have provided clues toward understanding this effect, but the underlying physical mechanisms for enhanced transmission are not yet fully clarified. Based on PH theory, I show that the microscopic origin of the nanohole plasmon resonance is a collective state formed by propagating thin film surface plasmons of wavelengths equal to integer fractions of the hole diameter. It is also shown that the hole plasmon resonance (HPR) depends strongly on the polarization of the incident light due to the optical coupling between antibonding film plasmon modes and perpendicularly polarized light to the film surface. The polarization dependency of HPR can be observed by using time-domain terahertz spectroscopy.

In Chapter 4, I discuss the coherent plasmon-exciton coupling between the local-

ized plasmons of a nanoshell and the excitons of molecular J-aggregates adsorbed on its surface in Au nanoshell/J-aggregate complexes, in which the properties of both the plasmon and the exciton are modified by their mutual interaction. The molecular adsorbates can modify the physical properties of nanoparticles by shifting their surface plasmon resonance,[28] or adsorbate properties such as fluorescence can be quenched or enhanced by the influence of a nanoparticle substrate.[29, 30] It has recently been shown that metallic nanoparticle-molecular adsorbate complexes can be designed that function as nanoscale pH meters[31], light harvesters[32], and optically responsive, active nanocomplexes[33]. Localized surface plasmons in nanoparticles are spatially confined and have significantly enhanced fields at the surface relative to the incident excitation field. This enhanced near field can strongly modify the properties of molecules, molecular complexes, or other excitonic systems, within the fringing field of the nanoparticle. Based on Gans theory and a Mie's calculation method, I calculate the optical absorption spectra of the plasmon-exciton hybridized states of the complex and compare the theoretical results with experimental measurements.

Chapter 5 discusses the plasmonic and optical properties of metallic tori using the PH method. I show that the plasmon resonances in a nanotorus result from hybridization of primitive plasmon modes that can be described as toroidal harmonics. The energies of the hybridized plasmon modes depend on the aspect ratio of the torus, which is defined as the ratio of the radius of the tube to the radius of the ring.

The plasmonic structure and optical absorption spectrum are found to be strongly dependent on the polarization. For polarization parallel to the ring, two distinct features appear in the absorption spectrum: A low intensity, high energy feature corresponding to the excitation of several higher order overlapping torus modes and a stronger low energy feature corresponding to dipolar plasmon oscillation in the plane of the ring. The energy of this resonance is strongly dependent on the aspect ratio of the torus. For aspect ratios smaller than 0.8, it is shown that the dipolar mode can be described analytically as an infinite cylinder plasmon of a wavelength equal to the circumference of the torus. For light polarized perpendicular to the ring, the spectra display two very closely spaced modes which can be interpreted as the bonding and antibonding combinations of two infinite cylinder plasmons of different azimuthal symmetry. The energies of these modes are only weakly dependent on the aspect ratio of the ring. The calculated optical properties are found to be in excellent agreement with results from numerical FDTD calculations.

In chapter 6, I summarize the main conclusions of previous chapters in this thesis. Based on plasmon hybridization theory, in chapter 2, I clarify the nature of plasmon modes of thin metal films and metallic nanoshell particles. In chapter 3, I explain the physical mechanism of the hole plasmon resonance in optical spectra for individual subwavelength holes in thin metal film. In chapter 4 and 5, I extend the plasmon hybridization theory to more complex structures of nanoparticles to analyze the optical

properties of thoes. The coherent coupling between the localized plasmons of a metallic nanoshell and the excitons of a J-aggregate molecules layer covering the metal gives rise to hybridized energies for plasmon-exciton coupling. The plasmon hybridization theory can also explain the optical properties of toroidal metal nanoparticles.

Chapter 2

Bonding and antibonding metallic film and nanoshell plasmons

2.1 Introduction

Metallic films and nanoshells are examples of tunable plasmonic nanostructures with important applications in waveguiding,[5, 34, 35] as nanoantennas,[7, 8, 36] metamaterials,[11, 12] chemical and biological sensing,[13, 14, 37] as light manipulators,[38] and biomedical applications.[15] Much recent work has been devoted to the metallic nanoshell where the plasmon resonance can be tuned very simply by varying the ratio of the shell thickness and overall radius.[2, 39, 40, 41, 42, 43, 44, 45, 46, 47, 48, 49]

For both structures, the plasmon modes can be expressed as linear combinations of the primitive plasmons associated with the two individual surfaces confining the metal. For a planar surface, the primitive plasmon mode is described by the two dimensional wavevector \vec{k} describing its propagation vector in the surface plane and for the spherical surface, the mode index is its multipolar symmetry (l, m) . In both the shell and film geometries, the interactions are diagonal in the mode indices resulting in hybridized bonding and antibonding plasmon modes of a common mode index.[50] The lower energy bonding plasmon mode is a symmetric alignment of the primitive plasmon modes associated with the two surfaces while the higher energy antibonding mode has an antisymmetric alignment. This alignment of surface charges

is counterintuitive since one would expect the Coulomb repulsion to be lower for an antisymmetric alignment.

2.2 Bonding and Antibonding Plasmon Modes

In this thesis I provide a simple physical explanation for why the symmetric alignment of surface charges results in a lower energy mode. This attractive interaction is a consequence of the incompressibility of the electron gas which results in the primitive plasmons associated with one of the surfaces also inducing secondary surface charges on the opposite side of the metal. The attractive interaction between the primary charges and secondary charges on the same surface is found to be larger than the repulsive interaction between primary charges on opposite surface thus favoring the symmetric alignment.

In the following we model the dielectric properties of the metals using a Drude Model (DM), $\epsilon(\omega) = 1 - \omega_B^2 / \omega(\omega - i\delta)$ with $\omega_B = 2.9$ eV and $\delta = 0.1$. Although this parameterization only provides a semi-quantitative description of the dielectric response of a real gold metal,[51] its simplicity reduces the complexity of the mathematical formalism used below. We have confirmed that all of the conclusions presented in this paper remain valid also for more realistic dielectric permittivities and arbitrary dielectric surroundings.

In Fig. 2.1 we show Mie calculations of the extinction spectrum, field enhancements and charge density amplitudes for a nanoshell of geometry (20,25) nm (inner

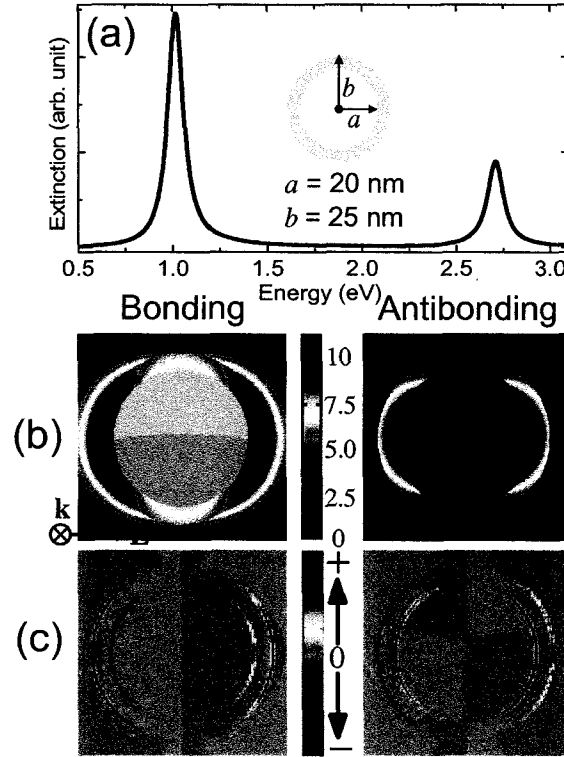


Figure 2.1 Mie calculations of the extinction spectrum (a), electric field enhancements (b) and charge density amplitudes (c) for the bonding 1.02 eV (left) and antibonding 2.71 eV (right) dipolar resonances of the nanoshell. The geometry of the nanoshell is (20,25) nm with dielectric data modeled using the DM.

radius 20 nm and outer radius 25 nm). The charge density amplitudes were obtained from the divergence of the electric field. The two features in the extinction spectrum of Fig. 2.1a are the bonding dipolar mode at 1.02 eV and the antibonding mode at 2.71 eV. The symmetric alignment of the surface charges for the bonding mode is apparent both in the field enhancement and charge density amplitude plots.

In Fig. 2.2, we show the dispersion relations, electric field profiles and charge distribution amplitudes for the plasmons of a thin film modeled using the DM and

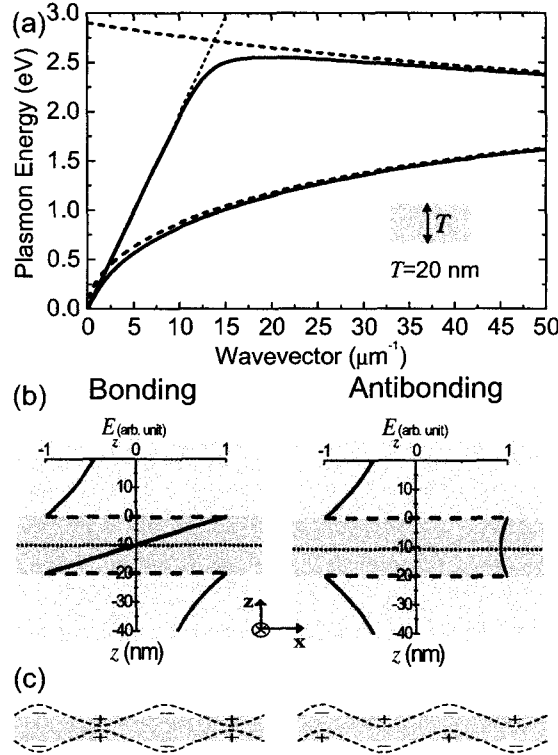


Figure 2.2 Exact retarded calculation of the bonding and antibonding film plasmon dispersion (a), electric field profiles (b) and schematic surface charge density distribution (c) for the bonding (left) and antibonding (right) film plasmon of wavevector $|\vec{k}|=40\text{ }\mu\text{m}^{-1}$. The film is modeled using the DM permittivity and the film thickness is $T=20\text{ nm}$. The dashed lines are the result from PH Eq. (2.5) and the red dotted line is the light line.

calculated using an exact electromagnetic approach.[52, 53, 54] The lower branch is the bonding film plasmon and the upper is the antibonding branch. For large wavevectors the splitting between the two plasmon branches increase with decreasing wavevector. For small wavevectors, the two branches interact strongly with the photon and exhibit an avoided crossing which push the energies of both film plasmon modes below the light line. As for the nanoshell, a symmetric alignment of the surface

charges for the lower energy bonding mode is apparent. The finding of a lower energy for the charge symmetric alignment of the film and nanoshell plasmon modes also applies for larger systems where retardation effects play a more dominant role.

We now proceed to investigate why the symmetric alignment of surface charge density results in a lower energy plasmon mode than the seemingly attractive antisymmetric alignment. In a fully retarded electromagnetic approach this becomes a very complicated task. However, as we will show below, the underlying physics emerges very clearly without unnecessary mathematical complications in the electrostatic limit. To do this we employ the Plasmon Hybridization (PH) method which is an exact analytical method for the description of plasmons in the nonretarded quasistatic limit.[1] The PH approach has been used previously to model nanoshell and film plasmons.[16, 20] For the small nanoshell discussed in Fig. 2.1, the PH method gives the same result as the Mie calculation and provide an exact description of the plasmons. For the thin film plasmons as shown in Fig. 2.2, the PH approach provides an accurate description for wavevectors larger than $20 \mu\text{m}^{-1}$ (wavelengths smaller than 300 nm) where retardation effects are negligible in the present geometry and DM for the metallic permittivity.

In the PH method, the plasmons are modeled as incompressible deformation of the electron fluid of uniform electron density n_0 constrained above a positive background provided by the metal ions. The physical deformation field of the conduction fluid can

be expressed as a gradient of a scalar potential η which satisfy Laplace equation.[16] In geometries where Laplace equation is separable, η can be expanded in a complete basis set, primitive plasmons, with time-dependent amplitudes. The normal modes are readily obtained from the Lagrangian of the system by application of Euler-Lagrange equations.

2.3 Film Plasmons

For a thin planar film of thickness T , η can be expanded as a sum of primitive plasmon modes of a common two-dimensional wavevector \vec{k} ,[20]

$$\eta_{\vec{k}} = \dot{P}_{\vec{k}}(t)e^{i\vec{k}\cdot\vec{\rho}+kz} + \dot{Q}_{\vec{k}}(t)e^{i\vec{k}\cdot\vec{\rho}-k(z+T)}, \quad (2.1)$$

where the amplitudes $P_{\vec{k}}$ and $Q_{\vec{k}}$ are the primitive surface plasmon mode amplitudes associated with the upper and lower film surfaces and the dots represent the time derivatives. The coordinates $\vec{\rho}$ and z refer to the lateral and perpendicular coordinates of the electron liquid in the film and $k = |\vec{k}|$. The interaction between the primitive plasmon modes is diagonal in \vec{k} ,[20] and this subscript will therefore be omitted in the following.

Each primitive plasmon induces surface charges on both surfaces of the film. The surface charge densities σ are obtained from, $\sigma = n_0 e \frac{\partial \eta}{\partial n}$ where \hat{n} is the surface normal vector and e is the charge of an electron. As illustrated in Fig. 2.3, the primitive plasmon mode P induce a primary surface charge of amplitude $\sigma'_P = en_0 k P$ on the

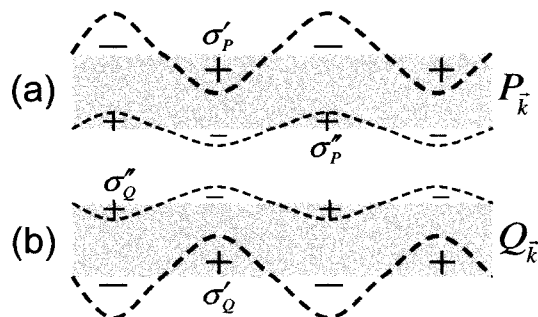


Figure 2.3 Illustration of the primary and secondary charge density distribution induced by the primitive plasmon modes $P_{\vec{k}}$ (a) and $Q_{\vec{k}}$ (b).

upper surface and a secondary surface charge of amplitude $\sigma''_P = -e^{-kT} \sigma'_P$ on the lower surface. Analogously, the primitive plasmon mode Q induces a primary surface charge $\sigma'_Q = en_0 k Q$ on the lower surface and a secondary surface charge $\sigma''_Q = -e^{-kT} \sigma'_Q$ on the upper surface. The electrostatic interaction between the surface charges can be evaluated analytically. The self interaction between the surface charges associated with the individual primitive plasmon modes P and Q leads to potential energies proportional to P^2 and Q^2 . The interaction between the two primitive plasmon modes can be expressed in terms of the instantaneous Coulomb interaction between the different surface charges as

$$V_{PQ} = V[\sigma'_P, \sigma'_Q] + V[\sigma'_P, \sigma''_Q] + V[\sigma''_P, \sigma'_Q] + V[\sigma''_P, \sigma''_Q], \quad (2.2)$$

where

$$\begin{aligned}
V[\sigma'_P, \sigma'_Q] &= 2\pi n_0^2 e^2 k e^{-kT} PQ \\
V[\sigma'_P, \sigma''_Q] = V[\sigma''_P, \sigma'_Q] &= -V[\sigma'_P, \sigma'_Q] \\
V[\sigma''_P, \sigma''_Q] &= e^{-kT} V[\sigma'_P, \sigma'_Q].
\end{aligned} \tag{2.3}$$

The Coulomb interaction between the two primary surface charges clearly is repulsive for a symmetric alignment of the primitive plasmon modes. However, the interaction between primary and secondary surface charges is attractive and counters this repulsive interaction and thus favors the symmetric alignment of surface charges observed in the bonding film plasmon modes. The Lagrangian for the primitive plasmon modes of wavevector \vec{k} takes the form,[20]

$$\begin{aligned}
L_{\vec{k}}^{Film} &= \frac{n_0 m_e}{2} k (1 - e^{-2kT}) \left[\dot{P}_{\vec{k}}^2 - \frac{\omega_B^2}{2} P_{\vec{k}}^2 \right. \\
&\quad \left. + \dot{Q}_{\vec{k}}^2 - \frac{\omega_B^2}{2} Q_{\vec{k}}^2 + \omega_B^2 e^{-kT} P_{\vec{k}} Q_{\vec{k}} \right],
\end{aligned} \tag{2.4}$$

where m_e is the effective mass of a conduction electron, and the bulk plasmon frequency, $\omega_B = \sqrt{4\pi n_0 e^2 / m_e}$. This Lagrangian can be diagonalized trivially by introducing the normal modes $M_{\vec{k}\pm} = (1/\sqrt{2})(P_{\vec{k}} \mp Q_{\vec{k}})$ where the subscripts $-$ and $+$ refer to charge-symmetric bonding and charge-antisymmetric antibonding modes. In the absence of background dielectrics, the energies of the film plasmon modes take the form:

$$\omega_{\vec{k}\pm} = \frac{\omega_B}{\sqrt{2}} \sqrt{1 \pm \exp(-kT)}. \tag{2.5}$$

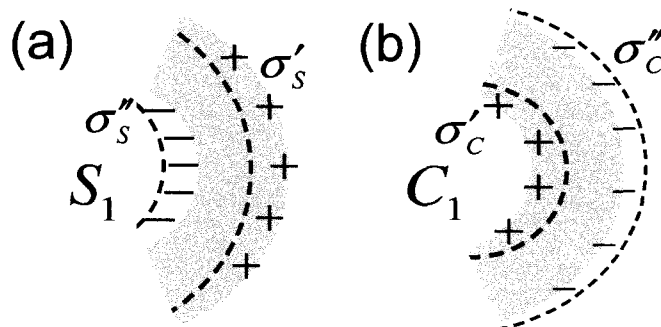


Figure 2.4 Illustration of the primary and secondary charge density distribution induced by a primitive dipolar ($l=1$) plasmon modes S_l (a) and C_l (b) for a nanoshell.

2.4 Nanoshell Plasmons

For a spherical metallic nanoshell of inner radius a and outer radius b , the scalar potential η can be expanded as a sum of primitive plasmon modes of a common multipolar index (l, m) , [16]

$$\eta_{lm}^{NS} = \left[\sqrt{\frac{1}{lb^{2l+1}}} \dot{S}_{lm}(t) r^l + \sqrt{\frac{a^{2l+1}}{l+1}} \dot{C}_{lm}(t) \frac{1}{r^{l+1}} \right] Y_{lm}(\Omega), \quad (2.6)$$

where $Y_{lm}(\Omega)$ is a spherical harmonic, and the amplitudes S_{lm} and C_{lm} refer to the primitive plasmon associated with the outer and inner shell surfaces respectively. As for the metallic film, the interaction between the primitive plasmon modes is diagonal in (l, m) . The plasmon energies do not depend on the azimuthal multipolar index m which therefore will be dropped in the following.

As illustrated in Fig. 2.4, the primitive plasmon mode S_{lm} induces a primary surface charge $\sigma'_S = en_0 \sqrt{\frac{l}{b^3}} S_l$ on the outer surface, and a secondary surface charge

$\sigma_S'' = -(\frac{a}{b})^{l-1}\sigma_S'$ on the inner surface. The cavity plasmon C_{lm} induces a primary surface charge $\sigma_C' = en_0\sqrt{\frac{l+1}{a^3}}C_l$ on the inner surface, and a secondary surface charge $\sigma_C'' = -(\frac{a}{b})^{l+2}\sigma_C'$ on the outer surface. As for the film, the electrostatic interaction between the surface charges can be evaluated analytically. The self interactions between the surface charges associated with each primitive plasmon mode gives potential energies proportional to S_l^2 and C_l^2 . The interaction between the two primitive plasmon modes can be expressed as a sum of the interaction between primary and secondary charges,

$$V_{SC} = V[\sigma_S', \sigma_C'] + V[\sigma_S', \sigma_C''] + V[\sigma_S'', \sigma_C'] + V[\sigma_S'', \sigma_C''], \quad (2.7)$$

where

$$\begin{aligned} V[\sigma_S', \sigma_C'] &= 2\pi n_0^2 e^2 \frac{\sqrt{l(l+1)}}{2l+1} \left(\frac{a}{b}\right)^{(l+1/2)} S_l C_l. \\ V[\sigma_S', \sigma_C''] &= V[\sigma_S'', \sigma_C'] = -V[\sigma_S', \sigma_C'] \\ V[\sigma_S'', \sigma_C''] &= \left(\frac{a}{b}\right)^{2l+1} V[\sigma_S', \sigma_C']. \end{aligned} \quad (2.8)$$

Thus, as for the metallic film, the repulsive interaction for a symmetric alignment of the primary charges is countered by a twice as large attractive interaction between the primary and secondary surface charges. This attractive interaction results in the mode with a symmetric alignment of surface charges having lower energy than the antisymmetric antibonding mode.

The Lagrangian for the primitive nanoshell plasmon modes of multipolar symme-

try (l, m) can be expressed as,

$$\begin{aligned}
L_l^{NS} &= \frac{n_0 m_e}{2} [1 - (\frac{a}{b})^{2l+1}] [\dot{S}_l^2 - \omega_{S,l}^2 S_l^2 \\
&+ \dot{C}_l^2 - \omega_{C,l}^2 C_l^2 + 2\omega_{S,l}\omega_{C,l}(\frac{a}{b})^{(l+1/2)} S_l C_l],
\end{aligned} \tag{2.9}$$

where $\omega_{S,l} = \omega_B \sqrt{\frac{l}{2l+1}}$ and $\omega_{C,l} = \omega_B \sqrt{\frac{l+1}{2l+1}}$. This Lagrangian can be diagonalized by introducing the normal modes $N_{l-} = \cos \xi_l C_l + \sin \xi_l S_l$ and $N_{l+} = \sin \xi_l C_l - \cos \xi_l S_l$, where $\tan \xi_l = \frac{\omega_{C,l}\omega_{S,l}}{\omega_{l+}^2 - \omega_{C,l}^2} (a/b)^{l+1/2}$. These modes correspond to the bonding charge-symmetric $(-)$ and antibonding charge-antisymmetric hybridized nanoshell modes of energies,

$$\omega_{l\pm}^2 = \frac{\omega_B^2}{2} \left[1 \pm \frac{1}{2l+1} \sqrt{1 + 4l(l+1) \left(\frac{a}{b}\right)^{2l+1}} \right], \tag{2.10}$$

and multipolar symmetry l .

2.5 Connection between Nanoshell and Film Plasmons

In this section, we show that in the electrostatic limit, the film plasmon dispersion Eq. (2.5) can be derived from the nanoshell plasmon modes Eq. (2.10) in the limit of a very large nanoshell of finite thickness T . The relation between the multipolar mode index l of spherical nanoshell plasmons and the propagation wavevector k of film plasmons is illustrated in Fig. 2.5 for the bonding modes. The situation is analogous for the antibonding modes. The surface charge density wave induced by a nanoshell plasmon of multipolar order l has $2l$ nodes along the circumference of the sphere. Thus for a nanoshell of geometry $(R - T, R)$ the physical length of a segment

with surface charge of the same sign is $L_l = 2\pi R/2l$. For a large radius R and large multipolar index l , this charge deformation is equivalent to a film plasmon of wavelength $\lambda_k = 2L_l = 2\pi R/l$. Since the relation between wavevector and wavelength for film plasmons is $\lambda_k = 2\pi/k$, the relation between l and k can be obtained directly from $\lambda_l = \lambda_k$, i.e. $l = Rk$. Inserting this multipolar index dependence on R and taking the limit $R \rightarrow \infty$ of Eq. (2.10) we obtain

$$\begin{aligned} \lim_{R \rightarrow \infty} \omega_{\pm}^2 &= \frac{\omega_B^2}{2} \left[1 \pm \sqrt{\lim_{R \rightarrow \infty} \left(\frac{R-T}{R} \right)^{2Rk+1}} \right] \\ &= \frac{\omega_B^2}{2} \left[1 \pm \exp(-kT) \right]. \end{aligned} \quad (2.11)$$

These plasmon energies corresponds exactly to the bonding and antibonding film plasmons of wavevector k obtained using Eq. (2.5).

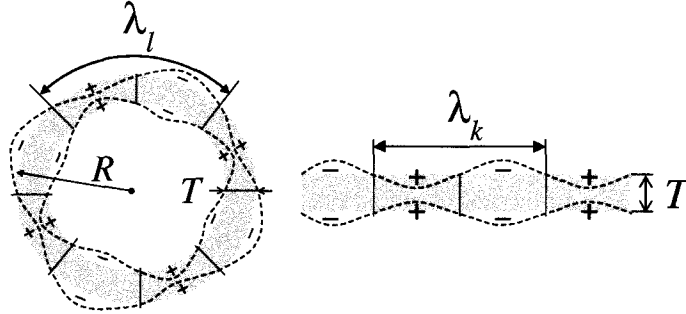


Figure 2.5 Illustration of the relation between the multipolar index l of a nanoshell plasmon and the wavevector k of a film plasmon. The surface charges induced by a bonding $l=4$ nanoshell plasmon can be viewed as a standing wave of a wavelength λ_l . In the limit of infinite radius and finite film thickness, this surface charge distribution is equivalent to the surface charge distribution of a bonding film plasmon of wavelength $\lambda_k = \lambda_l$.

We note that this derivation was performed in the electrostatic limit. Although we made use of the limit of infinitely large nanoshells, the relevant nanoshell plasmon modes were those of infinitely large multipolar index l which remain electrostatic since the instantaneous Coulomb interactions determining the energies of high multipolar index plasmon resonances of a nanoshell are local. At the moment we are unable to rigorously prove the equivalence between fully retarded film plasmon modes and finite thickness infinite diameter nanoshells plasmon modes.

2.6 Dielectric and Electrodynamic Effects on Film Plasmons

As we take into account the dielectric constant effects, the interacting potential energy term in the Lagrangian is modified to a screened form in terms of dielectric constants. The dispersion relations become

$$\omega_{k\pm} = \omega_B \sqrt{\frac{(\epsilon_0 + \epsilon_\infty) + (\epsilon_0 - \epsilon_\infty)e^{-2kT} \pm 2\epsilon_0 e^{-kT}}{(\epsilon_0 + \epsilon_\infty)^2 - (\epsilon_0 - \epsilon_\infty)^2 e^{-2kT}}} \quad (2.12)$$

where ϵ_0 is the dielectric constant of the background or vacuum and ϵ_∞ is the high frequency component of the dielectric function of the metal. In Fig. 2.6a, we show the dispersion relation of the thin metallic film in the electrostatic limit with $T=30$ nm, $\epsilon_0=1$, $\epsilon_\infty=9.5$, and $\omega_B=8.94$ eV to consider the Au film. For a very thick film, the plasmon frequency will have a constant value of the surface plasmon frequency ω_S ($=2.76$ eV) in which the background dielectric effect is included. However, as the thickness of the film becomes thinner, the interaction of the primitive plasmons on

the upper and lower surfaces increases and the film plasmon energies are split into bonding and antibonding modes.

The eigenmodes of the film plasmons can also be solved via MEs with boundary conditions for the given geometrical structure as Fig. 2.2.[52, 53, 54] Here, we only consider a transverse magnetic (TM) mode, in which the electric fields propagate in the \mathbf{x} -direction and are constrained at the interface between the film surface and the vacuum to the \mathbf{z} -direction. Therefore we make the following ansatz for the electric fields in three regions:

$$\mathbf{E} = \begin{cases} \mathbf{E}^u e^{-\gamma_0 z} e^{i(\mathbf{kx} - \omega t)} & ; z \geq 0 \\ (\mathbf{E}^{Fu} e^{\gamma_1 z} + \mathbf{E}^{Fl} e^{-\gamma_1(z+T)}) e^{i(\mathbf{kx} - \omega t)} & ; -T \leq z \leq 0 \\ \mathbf{E}^l e^{\gamma_0(z+T)} e^{i(\mathbf{kx} - \omega t)} & ; z \leq -T \end{cases} \quad (2.13)$$

where, $\mathbf{E}^u(\mathbf{E}^l)$ is the electric field of the upper (lower) film surface in vacuum sides, and $\mathbf{E}^{Fu}(\mathbf{E}^{Fl})$ is the electric field of the upper (lower) film surface in the film. The quantities γ_0 and γ_1 are the \mathbf{z} components of the wavevector in the vacuum and the film respectively, and have the form $\gamma_i^2 = k^2 - \epsilon_i(\omega/c)^2$; ($i = 0, 1$), which are given by inserting Eq. (2.13) to the MEs, where ϵ_1 is the dielectric constant of a metallic film. The dispersion relation of the film plasmons are calculated from the boundary conditions with the following form

$$\gamma_1 \epsilon_0 + \gamma_0 \epsilon_1 = \pm e^{-\gamma_1 T} (\gamma_1 \epsilon_0 - \gamma_0 \epsilon_1). \quad (2.14)$$

Fig. 2.6b shows the dispersion relations for the metallic film in vacuum. The $-$ sign of

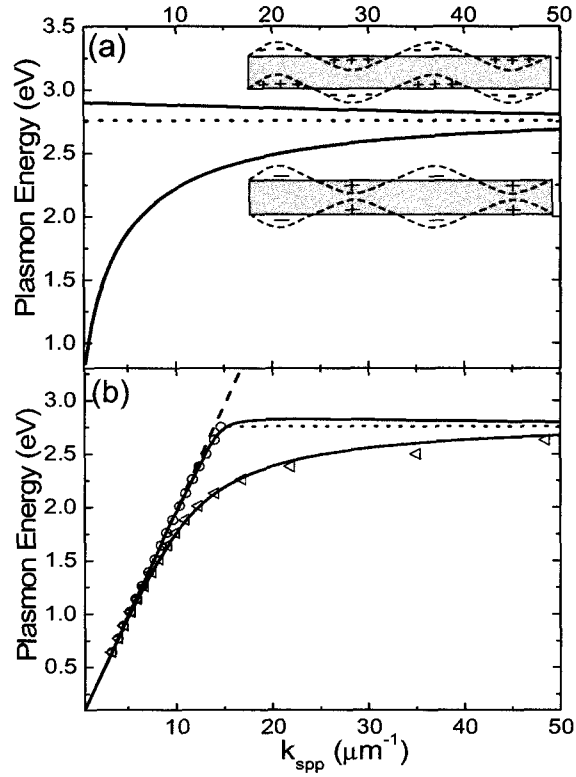


Figure 2.6 (a) Dispersion relations of film plasmons in the vacuum, obtained from the electrostatic limit expression Eq. (2.12). The upper solid line is the antibonding film plasmon mode and the lower solid line is the bonding film plasmon mode for $T=30$ nm, $\epsilon_0=1$, $\epsilon_\infty=9.5$, and $\omega_B=8.94$ eV. The dotted line is the surfaceplasmon energy (ω_S) including dielectric effect 2.76 eV ($= \omega_B/\sqrt{\epsilon_0 + \epsilon_\infty}$) as an electrostatic limit dispersion relation of SPPs for a thick metal film in the vacuum. The upper inset shows the charge distribution of antibonding mode and the lower inset shows the charge distribution of bonding mode. (b) Dispersion relations calculated using Eq. (2.14) for a thin metal film in the vacuum with full electrodynamics including the retardation effect. The upper solid line is the antibonding mode and the lower solid line is the bonding mode for $T=30$ nm, and $\epsilon_1(\omega) = \epsilon_\infty - \omega_B^2/\omega^2$. Opened circle (antibonding mode) and triangular (bonding mode) data points are calculated from the dielectric constants of JC data for Au. The dotted line is the dispersion relation of SPP for thick Au film, and the dashed line is the light dispersion in the vacuum as $\omega = ck$.

Eq. (2.14) gives the lower energy branch which corresponds to the bonding mode, and the $+$ sign gives the higher energy branch which corresponds to the antibonding mode. These two modes are split from the dispersion relation of a single interface, which is represented as a dotted line in Fig. 2.6b, as in the case of PH method. However the main difference of the dispersion relations by solving MEs and the PH method comes from the retardation effect. The dispersion relations of the film plasmons in Fig. 2.6b are put under the light dispersion line $\omega = ck$, which is represented by the dashed line, since the speed of light c is a finite value. In order to get the dispersion relations as solid lines, we used the dielectric function of a metal as $\epsilon_1(\omega) = \epsilon_\infty - \omega_B^2/\omega^2$ to mimic the dielectric functions for Au of the Johnson and Christy (JC) data, and opened circle and triangular data points are calculated by the real JC data.[51] In the electrostatic limit, the dispersion relations of Fig. 2.6b become Fig. 2.6a.

In order to compare the dispersion relations obtained by PH method and the solution of MEs more analytically, we take the non-retarded limit ($c \rightarrow \infty$) for the latter, where γ_0 and γ_1 become k , and $\epsilon_1(\omega) = 1 - \omega_B^2/\omega^2$ as in the Drude form. Then the eigen-frequencies are simply obtained from Eq. (2.14) as $\omega_\pm = \omega_S \sqrt{1 \pm \exp(-kT)}$ which are equivalent results with the PH method. We can further investigate the eigenmodes from the boundary condition for the normal components of the electric fields E_z^u and E_z^l , $E_z^l = e^{-\gamma_1 T} E_z^u (\epsilon_0/\epsilon_1 - \gamma_0/\gamma_1) / (\epsilon_0/\epsilon_1 + \gamma_0/\gamma_1)$. From the non-retarded limit and the Drude form of dielectric function for ϵ_1 , for the higher frequency

$\omega = \omega_+$, $E_z^l = E_z^u$ which means that the normal component of the electric fields on two interfaces of the film are aligned in the same direction as each other as in Fig. 1(a) and opposite charges are antisymmetrically distributed on the film surfaces as the upper inset in Fig. 2.2b. However for the lower frequency $\omega = \omega_-$, $E_z^l = -E_z^u$ and the normal components of the electric fields at two interfaces of the film are aligned in opposite directions of each other as Fig. 2.2a.

In the nonretarded quasi-electrostatic limit, the SPP may propagate infinitely without any loss, because the imaginary part of the SPP wavevector $\text{Im}[k_{spp}]$ is zero. However, in the realistic case, SPP propagate with finite distance because of the intrinsic damping and the ohmic loss. Therefore we calculated $\text{Im}[k_{spp}]$ as a function of plasmon energies numerically from Eq. (2.14) using both real and imaginary parts of dielectric constant for Au from JC data.[51] In Fig. 2.7, circular data points are $\text{Im}[k_{spp}]$ for the antibonding mode and triangular data points correspond to that of the bonding mode. The real part of k_{spp} for both of antibonding (lower dotted line) and bonding (upper dotted line) modes are plotted together with $\text{Im}[k_{spp}]$. The SPP propagation length of the antibonding mode is about 10 times longer than that of the bonding mode for the same plasmon energies, because the energy loss by the intrinsic damping of the bonding mode is larger than the ohmic loss of the antibonding mode. $\text{Im}[k_{spp}]$ of both bonding and antibonding modes diverge as the plasmon energy approach to the surface plasmon energy $\omega_S = 2.76$ eV, that SPP can not propagate

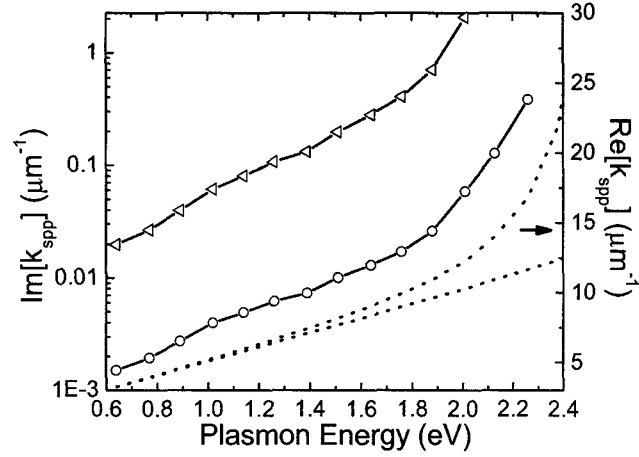


Figure 2.7 Imaginary part of the SPP wavevector ($\text{Im}[k_{spp}]$) as a function of the plasmon energy (left axis). Circular data point are for the antibonding mode, and triangular data points are for the bonding mode. All data points are calculated with same parameters as Fig. 2.6(b) and dielectric constants of JC data for Au. Dotted lines are same dispersion relations as Fig. 2.6(b) but we represent the SPP wavevector $\text{Re}[k_{spp}]$ as a function of the plasmon energy (right axis).

for the energies higher than ω_S .

2.7 Conclusion

Using simple and universal concepts we have provided an intuitive explanation for why the seemingly repulsive alignment of the surface charges associated with a bonding nanoshell and thin film plasmon results in plasmon modes of lower energy than the seemingly attractive antisymmetric alignment. We have also demonstrated that the plasmon dispersion for a thin metallic film can be derived from the expression for nanoshell plasmon energies in the limit of a large nanoshell of finite thickness. In addition, by considering retardation effect we have calculated the $\text{Im}[k_{spp}]$ numerically, and showed that the antibonding plasmon mode propagates 10 times longer than the

bonding mode. The main reason is that the intrinsic damping of the bonding mode is larger than the antibonding mode for the same energy.

Chapter 3

Optical Properties of a Subwavelength Hole in a Thin Metallic Film

3.1 Introduction

The optical properties of metallic nanostructures are a subject of considerable fundamental and technological importance. The excitation spectrum of a metallic nanostructure is determined by its plasmon resonances, which are collective oscillations of the conduction electrons. The energies of plasmon resonances can depend strongly on shape and composition of the nanostructure.[55, 56, 57, 58, 59, 60, 61] Examples of highly tunable plasmonic nanoparticles are metallic nanoshells[2] and nanorods.[3, 4] The tunability of the plasmon resonances of metallic nanoparticles can be exploited to position the optical resonances at specific wavelength regions of interest, and has led to a wide range of applications across many disciplines in science and engineering. In addition to their fundamental importance, plasmonic nanostructures are receiving a great deal of attention for their potential applications in areas such as subwavelength waveguiding,[62, 63] substrates for surface enhanced spectroscopies,[65, 64, 66, 67] sensing, biotechnology and biomedicine.[68, 69, 70, 71] The development of novel synthesis methods for nanostructure fabrication[72, 73, 74, 75] and new theoretical approaches for the understanding of their optical properties [77, 76, 78, 79, 80, 81] is making the field of nanophotonics an area of intense current interest.

Among various metallic nanostructures, a nanosized aperture, or nanohole, in a thin metal film has received particular attention since the discovery of the extraordinary optical transmission (EOT) phenomenon in nanohole arrays.[27, 82, 83] Near-field optical experiments have provided clues toward understanding this effect,[84, 86, 85] but the underlying physical mechanisms for enhanced transmission are not yet fully clarified.[87, 88, 89]

In order to fully understand the properties of complex systems such as nanohole arrays and single nanoholes of complex shape, one must first understand the most basic system, a single circular aperture in a thin metallic film. The optical properties of a single nanohole have been previously studied experimentally by other groups. The measured elastic scattering spectra have revealed that a hole plasmon resonance (HPR) is tuned to longer wavelengths by increasing the diameter of the hole.[90, 37] Near-field scanning optical microscopy (NSOM) experiments have shown that the hole acts as a scattering center for surface plasmon polaritons (SPPs).[37, 85] In the optical response of isolated holes, it has also been shown that the HPR wavelength is sensitive to its local dielectric environment and that the nanohole is useful for chemical and biological sensing applications.[90, 91, 92] Several studies of the optical properties of individual nanoholes in metallic films have been performed using numerical approaches with results that agree well with experimental findings. Finite-difference time-domain (FDTD) simulations have been used to elucidate the origins

of fringe patterns in films arising from the near field of a single nanohole,[85, 93] and the dependence of hole size and local dielectric environment on the light transmission and field enhancement of nanohole systems has been shown.[94] Boundary element method (BEM) has also been shown to reproduce the red-shifts of HPRs with increasing hole diameter using transmission calculations.[37] Other methods such as the multiple multipole (MMP) technique[95] and analytic calculations based on a normal-mode-decomposition technique[96] have shown that SPPs strongly enhance the light scattering with subwavelength apertures in a metallic thin film. However, a clear picture of the microscopic origin of the HPR and the strong dependence of its energy on hole size has not yet emerged.

In this thesis we provide a simple and physically intuitive picture of the HPR in a thin metallic film. In the thin film limit, the plasmons become symmetric and antisymmetric linear combinations of propagating surface plasmons localized on the upper and lower surfaces of the metal. In this case the plasmon dispersion depends strongly on the thickness of the film.[22] Using the Plasmon Hybridization (PH), method we show that the dispersion relations of the plasmon modes of a thin metallic film with a hole are the same as those of a continuous film. When the hole is present, the film plasmons can induce charges along the surface of the hole. Plasmon modes of corresponding spatial wavelengths can thus induce a dipole moment across the hole. These film plasmons, exposed by the presence of the hole, become optically active

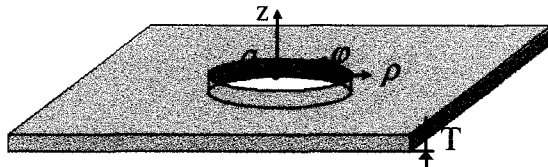


Figure 3.1 Schematic description of geometrical structure for a nanohole in thin film. T and a denote the film thickness and the hole radius respectively. Cylindrical coordinates (ρ, φ, z) are also represented.

and can be directly excited in contrast to the surface plasmon waves of a continuous film which require evanescent excitation.[22] It is these film plasmons rather than a localized hole-induced plasmon resonance that constitutes the HPR. Since the energies of thin film plasmons also depend on the thickness of the film, the energy of the HPR will also depend on film thickness. We verify this by measuring the scattering spectra of holes of fixed diameter in metallic films of varying thicknesses. To our knowledge, the film thickness dependence of the HPR has not been previously examined either experimentally or theoretically.

3.2 Theory

In the electrostatic limit, the nanohole in a thin metallic film system can be treated analytically using the Plasmon Hybridization (PH) method.[16, 20] The incompressible deformations of the electron gas in a film can be expressed in cylindrical coordinates (ρ, φ, z) , where the origin of the coordinate system is placed in the center of the hole with the z -axis perpendicular to the surface. The geometrical structure for the hole in a film is described in Fig. 3.1. The primitive plasmon of the system

are obtained from the scalar potential η

$$\eta = \frac{L^2}{(2\pi)^2} \sum_m \int dk k \left[\dot{P}(k, m, t) J_m(k\rho) e^{im\varphi} e^{kz} + \dot{Q}(k, m, t) J_m(k\rho) e^{im\varphi} e^{-k(z+T)} \right], \quad (3.1)$$

where L^2 is the area of the film surface, and J_m is a cylindrical Bessel function of order m . The quantities $\dot{P}(k, m, t)$ and $\dot{Q}(k, m, t)$ are the time derivatives of the primitive surface plasmon modes amplitudes of a wavevector k and azimuthal symmetry m associated with the upper and lower film surface. The hole does not need to be included in the expression for η , but will be included when calculating the kinetic and electrostatic contributions to the energy.

The Lagrangian for the primitive plasmons of the hole/film system is diagonal in m and can be written as,

$$\begin{aligned} L^m = & \int dk \int dk' \left[T_{k,k'}^{1,m} (\dot{P}(k) \dot{P}(k') + \dot{Q}(k) \dot{Q}(k')) + T_{k,k'}^{2,m} (\dot{P}(k) \dot{Q}(k') + \dot{Q}(k) \dot{P}(k')) \right] \\ & - \omega_{0s}^2 \left[V_{k,k'}^{1,m} (P(k) P(k') + Q(k) Q(k')) + V_{k,k'}^{2,m} (P(k) Q(k') + Q(k) P(k')) \right]. \end{aligned} \quad (3.2)$$

The kinetic energy $T_{k,k'}^{i,m}$ and the interaction energy $V_{k,k'}^{i,m}$ terms represent the propagation and scattering of a film plasmon of a wavevector k into another wavevector k' respectively. The kinetic energy terms can be written,

$$\begin{aligned} T_{k,k'}^{1,m} &= \delta(k - k') + \kappa_1(k, k'; a) + \kappa_3(k, k'; a) \\ T_{k,k'}^{2,m} &= \kappa_2(k, k'; a) + \kappa_4(k, k'; a), \end{aligned} \quad (3.3)$$

where

$$\begin{aligned}
\kappa_1(k, k'; a) &= \frac{k' \sinh\left(\frac{(k+k')T}{2}\right)}{(\sinh kT \sinh k'T)^{1/2}} \mathcal{J}_m(k, k'; a), \\
\kappa_2(k, k'; a) &= e^{kT} \kappa_1(k, k'; a), \\
\kappa_3(k, k'; a) &= \frac{ak'}{k+k'} \kappa(k, k'; a) \\
\kappa_4(k, k'; a) &= \frac{ak'}{k-k'} \kappa(k, k'; a) \\
\kappa(k, k'; a) &= J_m(ka) J'_m(k'a) \frac{\sinh\left(\frac{(k+k')T}{2}\right)}{(\sinh kT \sinh k'T)^{1/2}}, \tag{3.4}
\end{aligned}$$

where J'_m is the derivative of Bessel function, and

$$\mathcal{J}_m(k, k'; a) = \int_0^a d\rho \rho J_m(k\rho) J_m(k'\rho), \tag{3.5}$$

for the hole with radius a .

The total interaction energy is calculated by evaluating the product of the electrostatic potential and the induced surface charges $\sigma(\vec{r})$ on all surfaces of the system.[16]

The coefficients of the interaction energy take the form,

$$\begin{aligned}
V_{k,k'}^{1,m} &= \delta(k-k') - \gamma_0(k, k'; a) - \gamma_0(k', k; a) + \gamma_1(k, k'; a) + \gamma_3(k, k'; a) \\
V_{k,k'}^{2,m} &= -e^{-kT} \delta(k-k') + e^{-k'T} \gamma_0(k, k'; a) + e^{-kT} \gamma_0(k', k; a) - \gamma_2(k, k'; a) + \gamma_3(k, k'; a), \tag{3.6}
\end{aligned}$$

where

$$\begin{aligned}
\gamma_0(k, k'; a) &= \frac{\sqrt{1 - e^{-2kT}}}{\sqrt{1 - e^{-2k'T}}} k' \mathcal{J}_m(k, k'; a), \\
\gamma_1(k, k'; a) &= k' \int_0^\infty dp \mathcal{J}_m(p, k'; a) \mathcal{J}_m(k, p; a) \frac{(1 + e^{-(k'+k)T}) - e^{-pT}(e^{-kT} + e^{-k'T})}{\sqrt{(1 - e^{-2kT})(1 - e^{-2k'T})}}, \\
\gamma_2(k, k'; a) &= k' \int_0^\infty dp \mathcal{J}_m(p, k'; a) \mathcal{J}_m(k, p; a) \frac{e^{-pT}(1 + e^{-(k'+k)T}) - (e^{-kT} + e^{-k'T})}{\sqrt{(1 - e^{-2kT})(1 - e^{-2k'T})}}, \\
\gamma_3(k, k'; a) &= ak' \frac{(1 - e^{-k'T})J'_m(k'a)}{\sqrt{(1 - e^{-2kT})(1 - e^{-2k'T})}} [(1 - e^{-2kT})J_m(ka) \\
&\quad - k \int_0^\infty dp J_m(pa) \mathcal{J}_m(k, p; a) (1 - e^{-kT} - e^{-pT} - e^{-(p+k)T})].
\end{aligned} \tag{3.7}$$

In the absence of the hole, only the delta functions $\delta(k - k')$ remain in Eqs. (3.3) and (3.6) and the Lagrangian becomes diagonal in k and k' .

To solve for the plasmon modes, the degrees of freedom $P(k, m, t)$ and $Q(k, m, t)$ defined in Eq. (3.1) are discretized in \mathbf{k} -space. The Lagrangian is then converted to a quadratic form which can be solved by application of the Euler-Lagrange equations. The calculated dispersion relations for the hole/film system take the form of Eq. (3.12) and are unaffected by the hole.

However, the presence of the hole has a pronounced effect on the optical spectra because an incident light wave can couple to the dipolar component of the surface charges induced by the plasmon modes around the hole. The interaction of an incident multipolar external field and plasmons of the nanohole system takes the form,[16]

$$V_I^m = \int dS E_0(t) r^l Y_{lm}(\Omega) \sigma(\vec{r}), \tag{3.8}$$

where $E_0(t)$ is the time dependent electric field, and $Y_{lm}(\Omega)$ are spherical harmonics. In the dipolar limit for parallel polarization, one only needs to consider $l = 1$, and $m = \pm 1$. The surface integral (dipole moment) of Eq. (3.8) is calculated in the same way as for the kinetic and potential energy calculation, and results in

$$V_I^{\pm 1} = \int dk D(k) (P(k, \pm 1) + Q(k, \pm 1)) \quad (3.9)$$

where the dipolar coupling to the primitive film plasmons are

$$D(k) = Ca^2(1 - e^{-kT})(J_2(ka) + J_1'(ka)) \quad (3.10)$$

and C is a normalization constant. The frequency dependent dipolar polarizability is given by

$$\alpha(\omega) = \int dS r Y_{l=1,m}^*(\Omega) \sigma(\vec{r}) \quad (3.11)$$

and the optical absorption spectrum is obtained by taking the imaginary part of the polarizability as $\sigma(\omega) = \frac{\omega}{c} \text{Im}[\alpha(\omega + i\delta)]$, where the broadening parameter δ is proportional to the imaginary part of the dielectric function of the metal. The probability for excitation of a plasmon mode is proportional to the square of its dipole moment, $D(k)$. [50] For large k the dipole moment $D(k)$ vanishes as $1/k^{1.5}$ resulting in an effective incident light-plasmon coupling which decreases as $1/k^3$. To calculate the optical absorption, the interaction term Eq. (3.9) is expressed in our discrete basis and added to the Lagrangian which is then solved using matrix inversion. [16]

3.3 Experiment

The method for experimentally fabricating nanoholes is explained in detail elsewhere, [90] but briefly: Polystyrene spheres of a chosen diameter (desired diameter of nanoholes) are dispersed in a submonolayer onto a PDDA (polydiallyldimethylammonium chloride) functionalized glass slide. An Au layer of chosen thickness (here 20 nm, 30 nm, 40 nm, and 80 nm) is evaporated onto the slide. The polystyrene spheres are then removed from the surface by tape-stripping, leaving behind a random distribution of nanoholes in the Au film. Scattering spectra were obtained for individual nanoholes using dark-field microscopy.[90] A nanohole sample is brought into the focus of a 100X reflection dark-field objective (Zeiss). The image of the nanohole (a point source of light) is focused onto the slit of one of two imaging spectrometers (Acton, MicroSpec 2150i) selected by a beam splitter. One spectrometer is coupled to a CCD (Princeton Instruments, PhotonMax) for measurements at visible wavelengths, while the other spectrometer is coupled to a 1-D InGaAs array (Princeton Instruments, OMA V) for NIR measurements. Once the image of the nanohole is positioned in the slit of one of the spectrometers, a grating is shifted into place for spectral measurements. NIR and visible spectra were spliced during data processing. The spectra were corrected for the instrument's spectral efficiency using a white calibration standard (Edmund Optics), and a background spectrum of the Au surface, in the vicinity of the nanohole, was subtracted from each spectrum. Film thicknesses

measured by atomic force microscopy (Nanonics MV2000) were found to agree closely with thicknesses measured during evaporation (Sharon Vacuum e-beam evaporator).

3.4 Results and Discussion

3.4.1 Hole Plasmon Resonance for a Nanosized Hole

To understand the physical mechanism of the HPR, we start by analyzing the plasmonic properties and optical absorption of a hole in a thin perfect metallic film in vacuum, using a simple approach which neglects retardation effects. This analysis provides a simple and intuitive explanation of the microscopic origin of the HPR. Specifically, it predicts that for a fixed hole diameter, the energy of the HPR can be tuned by changing the thickness of the metallic film. The insight obtained from this simple model can then be used to analyze the optical properties of a more realistic system, i.e. a nanosized hole in a metallic film deposited on a substrate, modeled using realistic dielectric data and including retardation effects. Finally, our experimental study shows that the HPR can be tuned by changing the film thickness while keeping the hole diameter fixed.

In the methods section we use the PH method[16] to derive the film plasmon dispersion relation and an expression for the optical spectra of a hole of diameter D in a thin metallic film of thickness T . We show that the dispersion of film plasmons is unaffected by the presence of an individual hole. In an electrostatic approach such as the PH method, the optical properties of a nanostructure are scale invariant and can

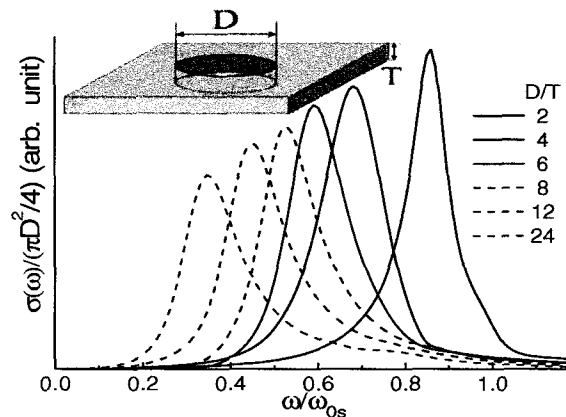


Figure 3.2 Dipolar optical absorption spectra of the hole/film system calculated by the plasmon hybridization (PH) method for different aspect ratios, i.e., the ratio of the diameter of the hole and the film thickness (D/T) probed by parallel polarization of incident light. The spectra are normalized by hole area. The aspect ratios are listed, in the key to the right, with color and line style corresponding to the respective spectrum. In the top inset, the geometrical structure for our calculation is displayed.

only depend on the structural parameters of the system as the aspect ratio D/T . In Fig. 3.2 we show the calculated absorption spectra for incident light perpendicular to the film for several different aspect ratios D/T . For a given aspect ratio, the spectrum is asymmetric and consists of a strong absorption feature at low energies, the HPR, and several weaker features at higher energies. The figure reveals a clear redshift of the HPR with increasing hole diameter.

In the PH method, the plasmon modes of the film are obtained as linear combinations of the surface plasmons associated with the upper and lower surfaces. The dispersion relation for the film plasmons is

$$\omega_{sp}(\vec{k}, \pm) = \omega_s \sqrt{1 \pm \exp(-|\vec{k}|T)}, \quad (3.12)$$

where \vec{k} is the two-dimensional propagation wavevector of the surface plasmon modes.[20] The $-$ sign denotes the bonding (B) film plasmon with symmetric alignment of surface charges on the top and bottom surfaces. The $+$ sign refers to the antibonding (AB) film plasmon with an opposite alignment of the surface charges. The charge alignment of the A and AB modes is illustrated in panels (a) and (d) in Fig. 3.3. The surface plasmon frequency is defined as $\omega_S = \sqrt{2\pi n_0 e^2 / m_e}$ where n_0 is the conduction electron density and m_e is the effective mass of a conduction electron.

The physical mechanism for the excitation of the HPR is illustrated in Fig. 3.3. In the dipole approximation, the coupling of light with surface plasmons is proportional to the square of the dipole moment of the plasmons. For this reason, light polarized parallel to the surface can couple only to B film plasmons. (Perpendicularly polarized light can couple to AB plasmons as shown in Fig. 3.3f.) On a continuous metallic surface, the plasmons possess no dipole moment. However, in the presence of a hole, the film plasmons can obtain a dipole moment due to the localized surface charges induced along the rim of the hole.

The optimal coupling between light polarized parallel to the surface occurs for film plasmons of half wavelength equal to the diameter of the hole,

$$k_{sp}^{opt} \sim 0.83\pi/D. \quad (3.13)$$

The numerical factor 0.83 is due to the transformation of the wavevector of a plane wave in Cartesian coordinates into cylindrical coordinates (diffraction), and is equal

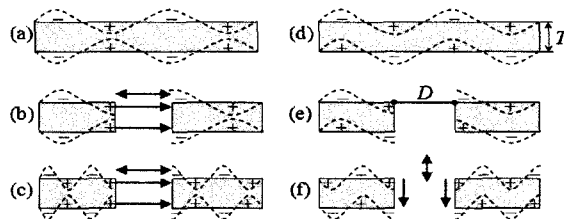


Figure 3.3 Charge configuration for Bonding (B) and antibonding (AB) film plasmon modes and the mechanism by which a nanohole allows coupling of light to these modes. (a) Symmetric charge modulation of B mode. (b) Optimal coupling between a B film plasmon mode and light of parallel polarization. (c) Coupling between a higher order B film plasmon mode and light of parallel polarization. (d) Antisymmetric charge modulation of AB mode. (e) No coupling between any AB film plasmon mode and light of parallel polarization. (f) Optimal coupling between an AB film plasmon mode and light of perpendicular polarization. Orange arrows represent the polarization direction of the incident light, and green arrows indicate the dipole moments resulting from the plasmon induced charges on the surfaces of the hole.

to the ratio of the wavevector for which a sine wave is maximum and the wavevector for which a cylindrical Bessel function of order one is maximum. The microscopic nature of the HPR in the electrostatic limit is thus a superposition of film plasmons centered at the wavevector given by Eq. (3.13).

As a result, we can expect a strong HPR at an energy

$$\omega_{HPR} = \omega_{sp}(k_{sp}^{opt}) = \omega_S \sqrt{1 - \exp(-0.83 \frac{\pi T}{D})}. \quad (3.14)$$

This expression is in perfect agreement with the results in Fig. 3.2 and shows clearly that the HPR will redshift both with increasing hole radius and with decreasing film thickness. While the redshift of the HPR with hole diameter is a simple geometric effect, the redshift with decreasing film thickness can be understood using simple electrostatics. For decreasing film thickness, the attractive electrostatic interaction

between the surface charges on the opposite sides of the hole increases.

Larger wavevector surface plasmons can also induce localized dipole moments across the hole as illustrated in Fig. 3.3c. The largest dipole moments are induced for plasmon wavelengths satisfying $k_{sp} = c_N \cdot (2N - 1)\pi/D$ where N is an arbitrary integer and c_N are the corresponding diffraction coefficients. These higher order plasmons give rise to absorption features at higher energies. However, the intensities of these features are strongly suppressed since the effective interaction with the incident field decays as the square of the dipole moment of the film plasmon Eq. (3.10), i.e., as $1/k^3$. Nonetheless, the spectra in Fig. 3.2 clearly reveal weak absorption features at larger energies than the HPR.

A more realistic system consisting of a nanosized hole in a thin metallic film on top of a glass substrate is schematically illustrated in the inset of Fig. 3.4b. To determine the energy of the HPR, we need to calculate the film plasmon dispersion relations including retardation effects and a realistic dielectric description of the materials.

For a metallic film on a substrate, the dispersion relations of the film plasmons can be calculated directly from the Maxwell equations in a planar geometry,[52, 54]

$$\begin{aligned} & \left(\frac{\epsilon_2}{\epsilon_1(\omega)} + \frac{\gamma_2(\omega)}{\gamma_1(\omega)} \right) \left(\frac{\epsilon_0}{\epsilon_1(\omega)} + \frac{\gamma_0(\omega)}{\gamma_1(\omega)} \right) e^{2\gamma_1(\omega)T} \\ &= \left(\frac{\epsilon_2}{\epsilon_1(\omega)} - \frac{\gamma_2(\omega)}{\gamma_1(\omega)} \right) \left(\frac{\epsilon_0}{\epsilon_1(\omega)} - \frac{\gamma_0(\omega)}{\gamma_1(\omega)} \right), \end{aligned} \quad (3.15)$$

where $\epsilon_i (i = 0, 1, 2)$ is the dielectric function in each region, i.e., vacuum, Au, and

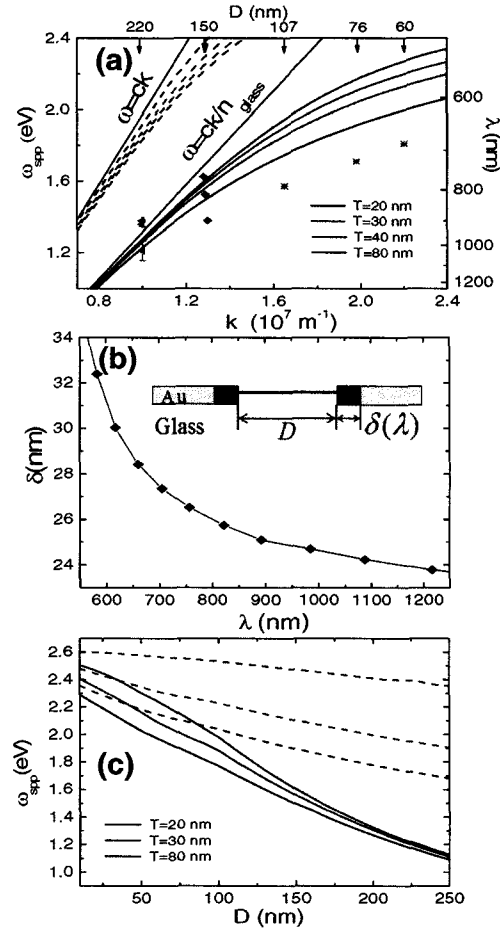


Figure 3.4 (a): Dispersion relations calculated using Eq. (3.15) for a nanohole in a thin metal film supported by a glass substrate for different film thicknesses: $T=20 \text{ nm}$ (red), 30 nm (green), 40 nm (blue), and 80 nm (violet). The upper branches are the antibonding (AB) film plasmon modes, and the lower branches are the bonding (B) modes. Solid lines are the bonding (B) modes, and dashed lines are leaky modes. The light lines for vacuum $\omega = ck$, and for glass $\omega = ck/n_{\text{glass}}$ are included as a guide to the eye. The HPR parameters deduced from the scattering spectra in Fig. 4 are shown in symbols: triangles ($D=220 \text{ nm}$), diamonds ($D=150 \text{ nm}$). The red stars denote the HPR parameters deduced from the experimental data for different D (scale on top of the figure) in Ref.[37] (b): Skin depth of Au ($\delta(\lambda)$) as a function of wavelength (λ) calculated using Eq. (3.16) and JC data. Inset: illustration of the penetration $\delta(\lambda)$ of the incident light. (c): Energies of HPR calculated using retarded (solid lines) and electrostatic (dashed lines) film plasmon dispersions as a function of hole diameter D and film thicknesses $T=20 \text{ nm}$ (red), 30 nm (green), 80 nm (violet).

glass respectively. This expression includes retardation effects. To model the gold film $\epsilon_1(\omega)$, we use the Johnson and Christy (JC) data.[51] For the glass substrate, we use a constant dielectric permittivity of $\epsilon_2 = 2.25$. The quantities γ_i are the perpendicular components of the wavevector and have the form $\gamma_i^2 = k^2 - \epsilon_i(\omega/c)^2$. The dispersion relation can be obtained analytically by solving Eq. (3.15); the imaginary part of ϵ_1 does not affect this solution as long as surface plasmon oscillations remain weakly damped.[54] Figure 3.3a shows the dispersion relations of metallic films of several thicknesses supported by a glass substrate. To emphasize that these plasmons are calculated using a fully retarded approach, we refer to the energies of these modes as surface plasmon polariton modes (SPP) with energies $\omega_{spp}(k)$. As in the electrostatic limit, for each wavevector two SPP modes corresponding to a symmetric and anti-symmetric alignment of the surface charges on the two surfaces of the film. For SPP modes in this geometry, the modes are classified as "bound" if the modes lie below the light line for glass and "leaky" if the modes lie below the light line for vacuum but above the light line for the glass substrate. For the small wavevectors shown in Fig. 3.4a, the antibonding modes are "leaky" i.e., bound at the metal/vacuum interface but radiative at the metal glass substrate interface. For larger wavevectors, these antibonding modes lie below the glass light line and are therefore bound at both interfaces.[37, 53]

For a realistic description of the interaction of light with a nanosized hole we also

need to include the penetration of light into the metal around the hole (Fig. 3.4b, inset). This penetration increases the effective size of the hole and alters the resonance condition of Eq. (3.13) obtained using the nonretarded PH method. A rigorous calculation of δ would require taking into account both quantum and cavity quantum electrodynamic effects. As a simple estimate of this effect, we assume that the penetration depth δ is equal to the conventional skin depth. For a planar geometry, the skin depth of a metal is equal to:

$$\delta(\omega) = \frac{\sqrt{2}c}{\omega} \left(\sqrt{\epsilon_R(\omega)^2 + \epsilon_I(\omega)^2} - \epsilon_R(\omega) \right)^{-1/2}, \quad (3.16)$$

where $\epsilon_R(\omega)$ ($\epsilon_I(\omega)$) is the real (imaginary) part of the dielectric function, ω is the angular frequency of the light, and c is the speed of light. The skin depth $\delta(\omega)$ for Au, calculated using JC data, is plotted as a function of wavelength in Fig. 3.4b. The graph shows that in the near infrared (NIR) light can penetrate the Au by as much as 20 ~ 35 nm. With the penetration depth included, the optimal coupling occurs for film SPP modes of wavevectors centered around

$$k_{spp}^{opt} = 0.83 \cdot \frac{\pi}{D + 2\delta(\omega_{HPR})}, \quad (3.17)$$

where $\omega_{HPR} = \omega_{spp}(k_{spp}^{opt})$. This equation predicts that the energy of the HPR can be directly obtained from the dispersion relation for the film SPP modes. We will refer to the parameters $(k_{spp}^{opt}, \omega_{HPR})$ as the HPR parameters. Using this approach we can now analyze results from a recent study of the effect of hole diameter D on the HPR of a

hole in an Au film of thickness $T=20$ nm.[37] The energies of this HPR measurements, along with our prediction for the SPP wavevector Eq. (3.17), are shown in Fig. 3.4a. The HPR parameters follow the dispersion curve well and provide support for our simple model for the excitation mechanism of the HPR. The deviations from the experimental data may be due to material parameters, our oversimplified expression for the penetration depth δ , or that the fabricated holes are not perfectly cylindrical. In this previous study they also directly measured a wavelength $\lambda_{SPP} \approx 285$ nm of the SPP mode excited by 633 nm laser light for a $D=60$ nm diameter hole. This result is in good agreement with Eq. (3.17), which predicts $k_{spp}^{opt} \approx 2.2 \times 10^7 \text{ m}^{-1}$ corresponding to a wavelength of 280 nm.

In Fig. 3.4c, we show the energy of the HPR as a function of hole diameter and film thickness. The figure directly shows the tunability of the HPR with these parameters. For comparison, we also show the results calculated using film plasmon dispersions determined using an electrostatic approach neglecting retardation. The effect of retardation is a redshift of the long wavelength film plasmons. This redshift results in a stronger dispersion of the film plasmon and thus a stronger dependence of the energy of the HPR on hole diameter. Retardation effects also decrease the coupling of the plasmon induced charges on the opposite surfaces of the film leading to a reduced film thickness dependence of the long wavelength bonding film plasmon modes. This is why the retarded calculation gives a weaker thickness dependence of

the HPR compared to the nonretarded calculation.

Figure 3.4 shows characteristic scattering spectra of individual holes of 220 nm and 150 nm diameter in Au films of varying thickness. These data clearly illustrate the predicted redshift of the HPR with decreasing film thickness. For $D=220$ nm, the HPR shifts from 897 nm to 1020 nm when the thickness of the film changes from 80 nm to 20 nm. For $D=150$ nm, the HPR redshifts from 755 nm to 900 nm as the thickness of the film is decreased from 40 nm to 20 nm. This figure also clearly shows the previously observed redshift of the HPR with hole diameter for constant film thickness.[90] As noted previously, the HPR spectra are significantly broader than individual nanoparticle spectra.[90, 37] We believe that this is due to the fact that a distribution of film SPP modes of wavevectors centered around the optimum film SPP wavevector k_{spp}^{opt} given by Eq. (3.17) can be excited. For an individual nanoparticle, only a distinct plasmon resonance is excited.

The energies of the HPR shown in Fig. 3.5 along with the corresponding wavevectors obtained using Eq. (3.17) are shown in the dispersion relations in Fig. 3.4a. The experimental data follow the theoretical predictions very well. For instance, not only does the HPR redshift with decreasing film thickness, but the magnitude of the shift is also smaller at higher energies, exactly as predicted by the dispersion relations. We also see the weak shoulders in the shorter wavelength (higher energy) region of the scattering spectra, which we believe may be due to excitation of higher order B modes.

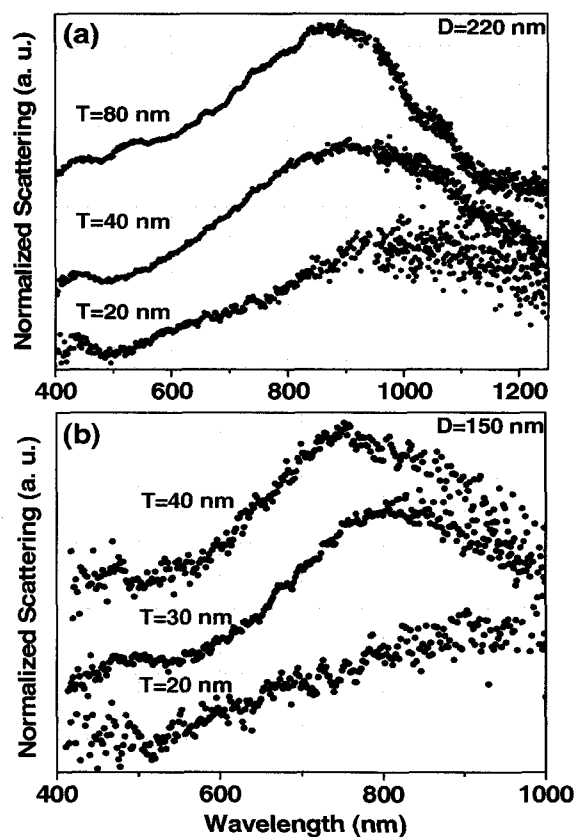


Figure 3.5 Experimental measurement of optical scattering for different hole/film systems. (a) individual nanoholes with diameter 220 nm and film thicknesses 80 nm, 40 nm, and 20 nm with corresponding peak positions at $\lambda_R = 897$ nm, 912 nm, and 1020 ± 54.6 nm. (b) individual nanoholes with diameter 150 nm and film thicknesses 40 nm, 30 nm, and 20 nm with corresponding peak positions at $\lambda_R = 755$ nm, 815 nm, 900 nm. Except for the $T=20$ nm and $D=220$ nm hole, the standard deviations of λ_R are less than 1.5%.

The experimental geometry also allows for the excitation of "leaky" antibonding film SPP modes, which should appear around 450 nm. These would be strongly damped due to interband transitions, which contribute below 500 nm. We believe that the small peak around 450 nm is most likely caused by interband transitions.

The present approach could in principle be extended to individual nanoholes of arbitrary shapes and to periodic hole arrays. For a single noncylindrical hole our finding that the plasmons of the film were unaffected by the presence of the hole would still apply. However, the hole would introduce couplings between SPP modes of different azimuthal symmetries m leading to excitations of SPP modes centered around several different wavevectors rather than around a single wavevector such as the simple resonance condition Eq. (3.17). For a periodic array of holes, the film SPP dispersion would no longer be unaffected by the holes but would exhibit bandgaps and other features characteristic of periodic structures. The description of such effects and their influence on the electromagnetic properties of hole arrays is better handled using numerical approaches such as the Finite-Difference Time-Domain or Finite Element methods.

3.4.2 Polarization Dependency

Based on the plasmon hybridization (PH) theory, it has been shown that the HPR is constituted by an induced dipole moment around the hole via incompressible surface charge deformation associated with the film plasmons.[97] For simplicity, when we

neglect the retardation effect, the film plasmons have two different modes in vacuum with energies $\omega_{\vec{k}\pm} = \omega_S \sqrt{1 \pm \exp(-kT)}$, where \vec{k} is a wavevector of surface plasmon modes, T is the film thickness, $\omega_S = \frac{\omega_B}{\sqrt{2}}$, and ω_B is the bulk plasmon frequency. $\omega_{\vec{k}-}$ ($\omega_{\vec{k}+}$) is the plasmon frequency of bonding (antibonding) mode which surface charge densities between the upper and lower surfaces of the film are symmetrically (antisymmetrically) aligned.[98]

The physical mechanism for the excitation of the HPR is illustrated in Fig. 3.6(c) and (d). In the presence of a hole, the light can couple with the film plasmons when the polarization of the light is parallel to the dipole moment induced around the hole. For parallel polarization, assuming the surface plasmon is a plane wave, the optimal coupling between light and the bonding mode surface plasmon occurs when half of the wavelength equals the diameter of a hole ($\lambda/2 \sim D$) as discribed in Fig. 3.6c. Whereas, perpendicularly polarized light couple to the antibonding film plasmons and the optimal coupling occurs when the wavelength of the surface plasmon equals the diameter of a hole ($\lambda \sim D$) as shown in Fig. 3.6d. However, when we consider the film surface as a two-dimensional plane, the surface plasmon propagating from the rim of the hole is described by a cylindrical Bessel function instead of the sinusoidal function. Therefore the optimal coupling conditions for the surface plasmon wavevector k_{sp} are given by $k_{sp} \sim 0.83\pi/D$ for the coupling between a bonding film plasmon mode and a parallel polarization light, and $k_{sp} \sim 2 \cdot 0.83\pi/D$

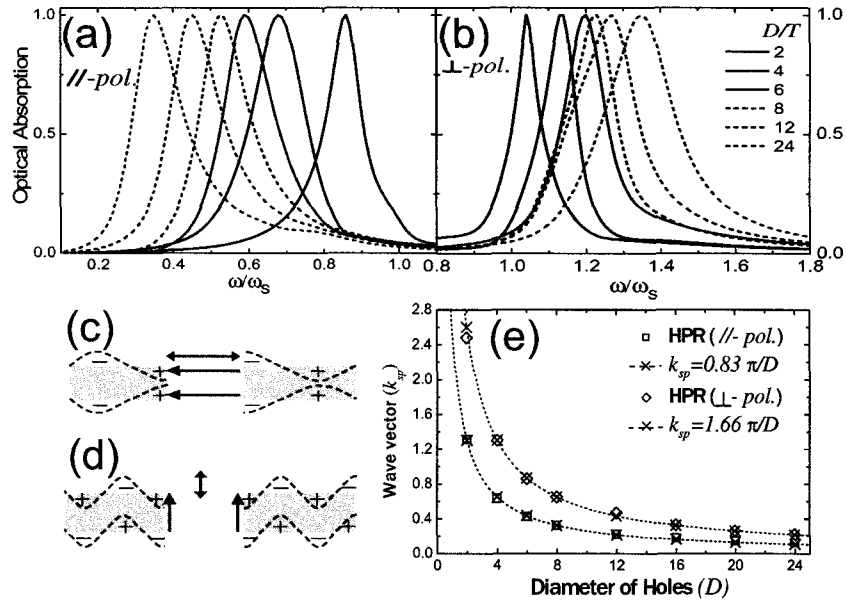


Figure 3.6 (a) Dipolar optical absorption spectra of the hole/film system calculated by the plasmon hybridization (PH) method for different size of the hole probed by parallel polarization of incident light. (b) Dipolar optical absorption spectra of the hole/film system calculated by the plasmon hybridization (PH) method for different size of the hole probed by perpendicular polarization of incident light. (c) Optimal coupling mechanism between parallel polarization light (orange arrow) and induced dipole moment (green arrow) around the hole by bonding film plasmon modes. Symmetric alignment of charge configuration for bonding modes is also described. (d) Optimal coupling mechanism between perpendicular polarization light and induced dipole moment around the hole by antibonding film plasmon modes. Antisymmetric alignment of charge configuration for antibonding modes is also described. (e) Comparison between PH method calculation and optimal coupling condition. Red (blue) color denotes the coupling between bonding (antibonding) modes and parallel (perpendicular) polarization light.

for the coupling between an antibonding mode and a perpendicularly polarized light.

In Fig. 3.6(a) and (b), we show the dipolar optical absorption spectra calculated by PH method for both parallel and perpendicular polarization of incident light and different aspect ratio D/T . For parallel polarization (Fig. 3.6a), the HPR exhibits a strong red shift with increasing hole diameter. We can also expect the resonance peak position around $\omega_{HPR\parallel} = \omega_S \sqrt{1 - \exp(-0.83\frac{\pi T}{D})}$ from the optimal coupling condition for a parallel polarization light and the film plasmon dispersion relation for bonding modes. For perpendicular polarization (Fig. 3.6b), the PH theory give rise to a little blue shift of HPR with increasing hole diameter. The resonance peaks are expected around $\omega_{HPR\perp} = \omega_S \sqrt{1 + \exp(-0.83\frac{2\pi T}{D})}$ from the optimal coupling condition for a perpendicular polarization light and the film plasmon dispersion relation for antibonding modes. However, this feature would be strongly suppressed if we consider the retardation effect for a realistic system. Fig. 3.6(e) shows that the HPR calculated by PH theory explain the optimal coupling condition very well. The square and diamond data points are surface plasmon wavevectors of bonding and antibonding modes obtained by inserting the HPR frequencies given by PH method calculation into the dispersion relation. Each data point shows accurate consistency with optimal coupling condition for given diameter of holes.

Experimentally, in the visible or infrared wavelength range of light, individual holes with nanometer scale of diameter have shown the strong red shift of HPR

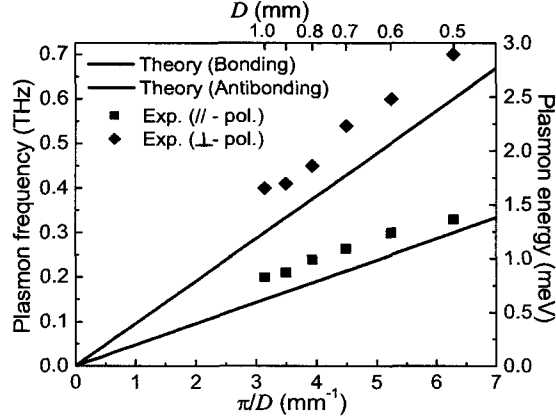


Figure 3.7 Comparison between theoretical expectation and experimental measurement of HPR. The red (blue) line denotes the theoretically predicted HPR frequencies associated with the bonding (antibonding) film plasmon modes as a function of hole diameters. Red square (blue diamond) data points are obtained by the peak positions of tera hertz spectra for different size of holes with parallel (perpendicular) polarization light.

with increasing the diameter or decreasing the film thickness for parallel polarization light.[97, 37, 90] The red shift could be explained theoretically in terms of bonding film plasmon mode very well. On the other hand, for the perpendicularly polarized light, in visible range, the HPR peak position expected by the antibonding mode is overlapped around the peak caused by interband transition. Thus we could not have strong evidence for the observation of antibonding mode. However, in the tera hertz frequency regime, the metal film can be regarded as nearly perfect conductor, and the retardation effect strongly affect to the dispersion relation of the thin film. Therefore, the dispersion relations of both bonding and antibonding modes become the light dispersion line ($\omega_{\vec{k}\pm} = ck$, where c is the speed of light in the vacuum.) regardless the film thickness. Even though the bonding and antibonding film plasmon energies

are degenerated in tera hertz regime due to the retardation effect, we believe that the plasmon hybridization between upper and lower film surfaces still exist in the thin film and the interaction between surface plasmons decays exponentially with increasing the film thickness as e^{-kT} . Therefore, based on our theoretical viewpoint for HPR, we expect that the HPR for both parallel and perpendicular polarization exhibit the red shift with increasing diameter of holes associated with the optimal coupling conditions. We have compared our theoretical prediction and the experimental data obtained from tera hertz spectra in Fig. 3.7. They show excellent consistency each other as we expected.

3.5 Conclusion

Using the plasmon hybridization approach, we have presented a simple physical explanation for the experimentally observed resonance in the optical spectra of nano-sized holes in thin metallic films. When the hole is present, the film plasmons induce charges on the surfaces of the hole. Film plasmons of certain wavelengths that depend on the diameter of the hole can induce a large dipole moment across the hole. The hole thus mediates a coupling between these specific film plasmons and an incident electromagnetic wave. A simple expression for the wavelength of the dipole active film plasmons is obtained. For increasing hole diameter, the wavelength of the dipole active film plasmons decreases resulting in a redshifted energy of the hole resonance. Our approach provides a quantitative explanation for the experimentally

observed redshift of a hole resonance as a function of hole diameter in previous experiments on films with fixed film thickness. We predict a redshift of the energy of the hole resonance with decreasing film thickness, which is substantiated in experimental measurements on individual nanoholes.

Chapter 4

Plasmon-Exciton Coupling in Nanoshell/J-Aggregate Complexes

4.1 Introduction

Metallic nanoparticles in combination with molecular adsorbates provide one of the most adaptable architectures for the design and implementation of functionality at the nanoscale. The molecular adsorbates can modify the physical properties of nanoparticles by shifting their surface plasmon resonance,[28] or adsorbate properties such as fluorescence can be quenched or enhanced by the influence of a nanoparticle substrate.[29, 30] It has recently been shown that metallic nanoparticle-molecular adsorbate complexes can be designed that function as nanoscale pH meters[31], light harvesters[32], and optically responsive, active nanocomplexes[33]. Localized surface plasmons in nanoparticles are spatially confined and have significantly enhanced fields at the surface relative to the incident excitation field. This enhanced near field can strongly modify the properties of molecules, molecular complexes, or other excitonic systems, within the fringing field of the nanoparticle. To date, strong plasmon-exciton coupling has been observed in metallic films with propagating plasmons,[99, 100] and in complex geometries where both propagating and localized plasmons both contribute to the overall interactions of the system.[101, 102] while coherent plasmon-exciton coupling has been observed between the fixed-frequency localized plasmons

in Ag nanospheres and molecular J-aggregates.[103]

In this thesis, the plasmonic nanostructures used were Au nanoshells, tunable plasmonic nanoparticles consisting of a spherical silica core coated with a thin, uniform Au layer.(15) By varying the core size/shell thickness ratio, the plasmon energies of the nanoparticle can be systematically modified,(16, 17) and can be tuned through the exciton energy of the J-aggregate. This allows for the direct measurement of the coupling energy of the nanoshell-J/aggregate complexes. In section 4.2, based on Gans theory and a Mie's calculation method,I illustrate how to calculate the optical absorption spectra of the plasmon-exciton hybridized states of the complex and analyze the coupling strength of the hybridized states theoretically. I describe the experimental method in section 4.3, and discuss the experimental results with theoretical calculation. Then I conclude the coherent plasmon-exciton coupling in section 4.4.

4.2 Theory

In order to describe the nanoshell/J-aggregate complexes system, we consider a concentric three-layer model consisting of a two-layer spherical shell particle surrounded by a layer of J-aggregate (Fig. 4.1). ϵ_1 and ϵ_M are dielectric constants of the core with radius a and background media, respectively. ϵ_2 is a dielectric constant of the Au shell with radius b and the optical response is described by the Johnson and

Christy (JC) data [51] for realistic case or the Drude model

$$\epsilon_2(\omega) = \epsilon_\infty - \frac{\omega_p^2}{\omega^2 + i\Gamma\omega}, \quad (4.1)$$

where, ω is the frequency of incident field, ω_p is the bulk plasmon frequency, Γ is the collision rate of electrons in Au, and ϵ_∞ is the high frequency component of the Au dielectric function. ϵ_3 is a dielectric constant of the J-aggregate dye molecule covering the Au nanoshell with radius c . Optical response of ϵ_3 is phenomenologically obtained by the extinction spectra (Fig. 4.2) and the spectra is fitted well by Lorentzian line shape with an exciton energy $\omega_0 \sim 1.8$ eV (690 nm)

$$\epsilon_3(\omega) = \epsilon_{\infty J} - f \frac{\omega_0^2}{\omega^2 - \omega_0^2 + i\gamma\omega}, \quad (4.2)$$

where, f is the strength constant of the exciton signal with around $0.01 \sim 0.03$ from the best fit, γ is the half width at half maximum (HWHM) of the exciton peak and $\epsilon_{\infty J}$ is the high frequency component of the J-aggregate dye molecular dielectric function.

First, we compute the optical spectra using Mie scattering theory, which solves the vector wave equations of a time-harmonic electromagnetic field (E,H) derived from the Maxwell equations. [104] In the Mie theory calculation, in order to compare with experiment, we use JC parameter for the dielectric constant of Au and for the dye molecule we take $\epsilon_{\infty J} = 1$, $f = 0.02$, and $\gamma \sim 0.052$ as the best fitting parameters. The core of the nanoshell is silica that we use $\epsilon_1 = 2.04$, and the dielectric constant of

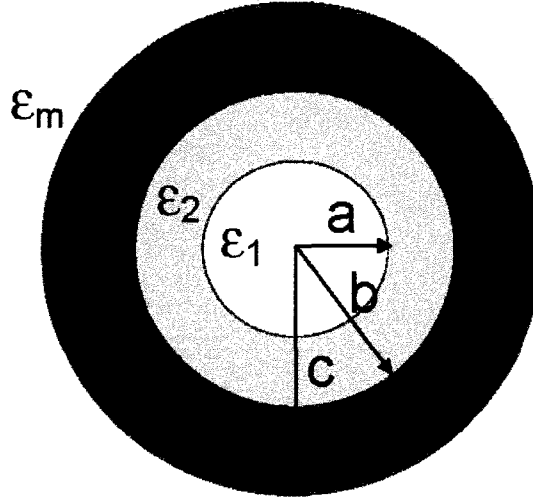


Figure 4.1 Schematic description of gold nanoshell/J-aggregate complex model for theoretical calculation. ϵ_1 , ϵ_2 , ϵ_1 , and ϵ_M represent silica core, gold shell, J-aggregate molecular layer, and surrounding medium, respectively. The core radius (a), nanoshell radius (b), and nanoshell/J-aggregate total radius of the complex (c) are shown.

water media $\epsilon_M = 1.77$. For the metallic nanoshell, it is well known that the localized surface plasmon resonance frequency can be tuned by varying the aspect ratio of inner and outer radii of the shell. Therefore, in principle, the plasmon frequency can be scanned through the exciton mode frequency. Fig. 4.4b,d show results of Mie scattering theory for dipole nanoshells and nanoshell/J-aggregate complexes, while Fig. 4.5b,d show the quadrupole nanoshell-based complex. Mie theory calculations accurately reproduce the experimental extinction spectra for both nanoshells and nanoshell/J-aggregate complexes. This implies that the coupling of plasmons and excitons can be microscopically understood in the classical electromagnetic context.

Next, we apply Gauss theory to analyze the nanoshell-J-aggregate complexes sys-

tem. However, Gans theory probes only the dipolar component of plasmon modes because it is quasielectrostatic approximation. The electric potential of the concentric two-layered spherical shell particle of Fig. 4.1 in the uniform external electric field along the arbitrary one direction is calculated by solving Laplace's equation associated with boundary conditions. Then, the polarizability α of this system is obtained from the induced dipole moment divided by the external field.[105] This is expressed as

$$\alpha = 4\pi\epsilon_0 c^3 \frac{\epsilon_{eff} - \epsilon_M}{\epsilon_{eff} + 2\epsilon_M}, \quad (4.3)$$

where

$$\begin{aligned} \epsilon_{eff} &= \epsilon_3 \frac{A - 2\left(\frac{b}{c}\right)^3 B}{A + \left(\frac{b}{c}\right)^3 B}, \\ A &= (2\epsilon_3 + \epsilon_2)(2\epsilon_2 + \epsilon_1) + 2(\epsilon_3 - \epsilon_2)(\epsilon_2 - \epsilon_1) \left(\frac{a}{b}\right)^3, \\ B &= (\epsilon_3 - \epsilon_2)(2\epsilon_2 + \epsilon_1) + (\epsilon_3 + 2\epsilon_2)(\epsilon_2 - \epsilon_1) \left(\frac{a}{b}\right)^3, \end{aligned} \quad (4.4)$$

and ϵ_0 is the permittivity of free space.

The polarizability becomes frequency dependent after substituting the expressions for ϵ_2 and ϵ_3 from Eq. (4.1) and Eq. (4.2) into Eq. (4.5). The optical absorption ($\sigma(\omega)$) is then calculated from the frequency dependent polarizability ($\alpha(\omega)$) by the following formula:

$$\sigma(\omega) = \omega \text{Im} [\alpha(\omega)]. \quad (4.5)$$

For an analytical model, we use the following Drude parameters: $\epsilon_\infty = 9.5$, $\omega_p = 9.0$ eV, $\Gamma = 0.5$ eV for Au nanoshell and the Lorentzian parameters as $\epsilon_{\infty J} = 1$, $f = 0.02$, $\gamma = 0.05$ for J-aggregate dye molecule. The new resonance frequencies ($\omega_{1\pm}^\pm$) are calculated from the equation $\frac{d\sigma(\omega)}{d\omega} = 0$ associated with Gans theory. These new resonant modes correspond to plasmon/exciton hybrid states resulting from the hybridization of the symmetric Au-nanoshell dipolar plasmon mode (ω_{1-}) and the resonant exciton mode (ω_0). As clearly shown in Fig. 4.4e, Gans theory results are very similar to the results from experiment and from Mie scattering theory. Note that the theoretical dispersion curves are obtained in a similar manner as the experimental dispersion curves.

In order to estimate the coupling strength between plasmons and excitons analytically, we need to simplify the model parameters. For instance, by fully considering the dielectric effects, even the dipolar nanoshell plasmon modes are very complicated as

$$\omega_{1\pm}^2 = \frac{\omega_p^2}{2} \frac{C_1}{C_2}, \quad (4.6)$$

where

$$\begin{aligned} C_1 &= \epsilon_1 + 4\epsilon_\infty + 4\epsilon_M - 2(a/b)^3(2\epsilon_\infty - 2\epsilon_M - \epsilon_1) \\ &\quad \pm \sqrt{(\epsilon_1 - 4\epsilon_M)^2 + 4(a/b)^6(\epsilon_M - \epsilon_1)^2 + 4(a/b)^3(\epsilon_1^2 + 13\epsilon_1\epsilon_M + 4\epsilon_M^2)} \\ C_2 &= (2\epsilon_M + \epsilon_\infty)(\epsilon_1 + 2\epsilon_\infty) - 2(a/b)^3(\epsilon_M - \epsilon_\infty)(\epsilon_1 - \epsilon_\infty). \end{aligned}$$

A simple analytical model for the coupling between the exciton and the plasmon can be derived by assuming that $\epsilon_\infty = \epsilon_M = \epsilon_1 = 1$. In this limit, the tunable plasmon frequencies of Au nanoshells are

$$\omega_{l\pm}^2 = \frac{\omega_p^2}{2} \left[1 \pm \frac{1}{2l+1} \sqrt{1 + 4l(l+1) \left(\frac{a}{b}\right)^{2l+1}} \right], \quad (4.7)$$

where l is the order of spherical harmonics, and $l = 1$ is dipolar component, $l = 2$ is quadrupolar, $l = 3$ is octupolar etc., and the $-(+)$ represents symmetric (anti-symmetric) coupling mode.[1] By varying the ratio a/b , the symmetric Au-nanoshell dipole plasmon mode

$$\omega_{1-} = \frac{\omega_p}{\sqrt{2}} \left(1 - \frac{1}{3} \sqrt{1 + 8 \left(\frac{a}{b}\right)^3} \right)^{1/2} \quad (4.8)$$

is tuned across the resonant exciton transition mode (ω_0) as shown experimentally and theoretically in Fig. 4.4a,b. The interaction between ω_{1-} and ω_0 results in the formation of new modes (plasmon/exciton hybrid states) which we denote here by ω_{1-}^\pm . The frequencies of these new states can be approximately obtained by equating the real part of the denominator of $\alpha(\omega)$ to zero and solving the roots in the limit where Γ and γ approach zero. Using this method, we obtain

$$(\omega_{1-}^\pm)^2 = \frac{1}{2}(\omega_0^2(1+f) + \omega_{1-}^2) \pm \frac{1}{2}\sqrt{(\omega_0^2 - \omega_{1-}^2)^2 + \omega_0^4 D^2}, \quad (4.9)$$

where

$$D^2 = f \left[(2+f) + \frac{2}{3} \left(1 - 4 \left(\frac{b}{c}\right)^3 \right) \frac{\omega_{1-}^2}{\omega_0^2} \right]. \quad (4.10)$$

In the hybridization scheme, D^2 can be regarded as a coupling term. We can generally interpret the coupling of Au-nanoshell plasmons and excitons from Eq. (4.10). The coupling strength increases as f and c increase, and does not change significantly for a very thick J-aggregate layer. On the other hand, the coupling strength decreases as f tends toward zero or as c approaches b . Therefore, the magnitude of splitting, $|\omega_{1-}^+ - \omega_{1-}^-|$, is controlled by the exciton oscillator strength and the thickness of the J-aggregate molecular layer.

4.3 Experiment

Nanoshells with a core radius $r_1 = 45$ nm, resulting in a dipolar plasmon resonant with the J-aggregate exciton line, and nanoshells with a larger core radius $r_1 = 90$ nm, with its quadrupolar plasmon resonant with the J-aggregate exciton, were designed and fabricated.

The J-aggregate used in these experiments is formed from the dye 2,2'-dimethyl-8-phenyl-5,6,5', 6'-dibenzothiacarbocyanine chloride, a system having high oscillator strengths and narrow transition line widths, suitable for achieving strong coupling at room temperature. The J-aggregate form of this dye has been well-studied in coupling with other systems, such as cavity photons[106, 107, 108, 109] and propagating plasmons.[99] A 0.5 mM solution of dye (2,2'-dimethyl-8-phenyl-5,6,5', 6'-dibenzothiacarbocyanine chloride) in a mixture of water/ethanol (50/50 by volume) was used throughout the experiment (Fig. 4.2a, inset). Addition of a polyvinyl alco-

hol solution transforms the dye to its J-aggregate form. Fig. 4.2a shows extinction spectra of 6 μL of the dye solution in 3.5 mL of water (black) and aqueous polyvinyl alcohol (red). The J-aggregate form of this dye has a narrow line width of nominally 20 nm and an absorption band that is red-shifted to 693 nm[99] relative to the monomer peak absorbance at 547 nm. The peak at 593 nm (black) is due to J-aggregate formation in solution resulting from the presence of ethanol.

Au nanoshells were fabricated as previously reported.[110] Nanoshells are parametrized by the inner core and outer shell radii $[r_1, r_2]$. In Fig. 4.2b,c, the extinction spectra of $[r_1, r_2] = [45, 63]$ nm nanoshells, and $[r_1, r_2] = [90, 120]$ nm nanoshells, respectively, are shown (red curves). The nanoshells are fabricated such that the dipole and quadrupole plasmon resonance energies are nearly degenerate with the J-aggregate absorption band. The $[r_1, r_2] = [45, 63]$ nm nanoshells possess a strong dipole plasmon resonance at 680 nm and a weaker quadrupole plasmon resonance, seen as a small shoulder that appears at 570 nm. The $[r_1, r_2] = [90, 120]$ nm nanoshells have a strong quadrupole plasmon resonance at 680 nm along with a dipole plasmon at 950 nm.

The extinction spectra for nanoshells shown in Fig. 4.2 (red curves) were obtained directly prior to the formation of the nanoshell/J-aggregate complex. To assemble the complexes, a volume of dye solution is added to an aqueous solution in which Au nanoshells are suspended, and mixed well by shaking. The solution is then allowed

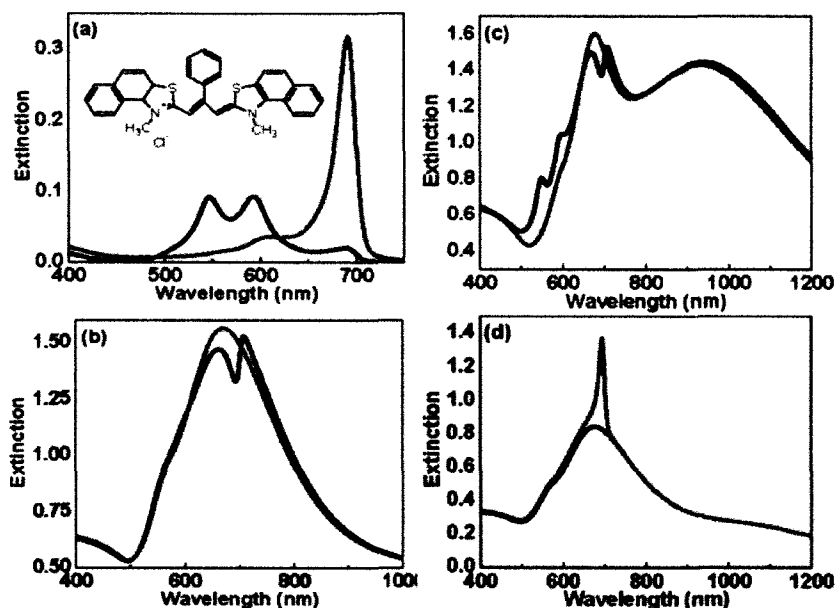


Figure 4.2 (a) Black: extinction spectrum of dye solution in 50/50 water/ethanol by volume. The peak at 547 nm is due to dye monomers while the peak at 593 nm results from aggregates induced by the presence of ethanol. Red: transformation of dye monomers to J-aggregates with absorption at 693 nm when 6 μL 0.5 mM dye solution is added to 3.5 mL of aqueous polyvinyl alcohol. Inset: structure of the organic molecule 2,2'-dimethyl-8-phenyl-5,6,5',6'-dibenzothiacarbocyanine chloride. (b) Red: extinction spectrum of aqueous solution of $[r_1, r_2] = [45, 63]$ nm nanoshells with peak dipole plasmon resonance wavelength at 680 nm. Black: extinction spectrum of 3.5 mL of aqueous nanoshell solution to which 6 μL of 0.5 mM dye solution is added, revealing two hybrid peaks of almost equal intensity. (c) Red: extinction spectrum of aqueous solution of $[r_1, r_2] = [90, 120]$ nm nanoshells with quadrupole plasmon resonance wavelength at 680 nm and dipole resonance at 950 nm. Black: 12 μL of dye solution added to 3.5 μL of nanoshell solution results in two hybrid peaks. The peaks at 547 and 593 nm can be correlated to the peaks in the black curve in (a). (d) Black: extinction spectrum of nanoshell solution. Red: nanoshell and dye solution absorption in tandem cell.

to sit for at least 45 min, after which the extinction spectrum is measured. The resulting extinction spectra are shown in Fig. 4.2b,c (black curves). The dipole and quadrupole plasmon peaks shown are strongly modulated by the presence of the J-aggregates and have been transformed into two new peaks separated by a dip at 693 nm, which corresponds to the maximum absorption wavelength of the J-aggregate.

Several control experiments were performed to confirm the formation of the nanoshell/J-aggregate complex. In one experiment, separate solutions of nanoshells and J-aggregates were examined by UV-vis spectroscopy in a tandem cell (STARNA) where the beam path traverses the two separate solutions sequentially. J-aggregates were obtained as before, by mixing the dye solution with an aqueous polyvinyl alcohol solution, but not in the presence of nanoshells. The extinction spectrum from the tandem cell, shown in Fig. 4.2d, appears to be the direct addition of the nanoshell extinction spectrum and the J-aggregate dye extinction spectrum, quite distinct from the distorted line shape observed in the plasmon line width of the nanoshell/J-aggregate complexes (Fig. 4.2b,c). This experiment confirms quite definitively that the spectra shown in Fig. 4.2b,c do not arise simply from the additive extinction of nanoshells and J-aggregates isolated from each other, but instead are directly the result of plasmon-exciton coupling.

The nanoshell/J-aggregate complexes appear to be formed through electrostatic self-assembly, due to the positively charged dye molecules and the nanoshell surfaces

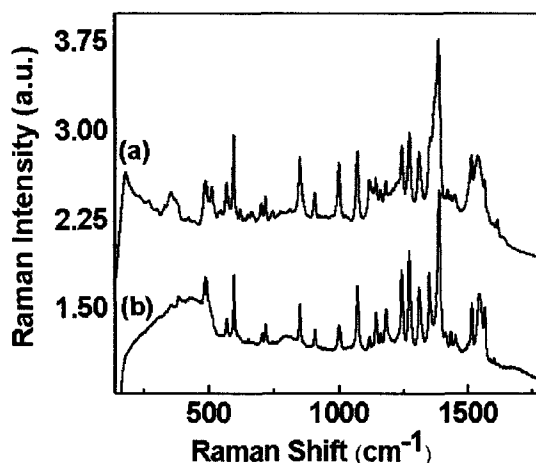


Figure 4.3 (a) SERS and (b) normal Raman spectra of 2,2'-dimethyl-8-phenyl-5,6,5',6',-dibenzothiacarbocyanine chloride.

that possess a net negative charge. It is quite possible that the J-aggregate complex formation in the presence of nanoshells may be initiated by this electrostatic attraction with the nanoshell surface. Following the mixing of nanoshells with dye solution, the peak transformation shown in Fig. 4.2b and c from the red spectra to the black spectra progresses for 45 min, when it reaches its final, coupled state with no further changes in the extinction spectra. The resulting complexes appear to be remarkably stable: samples preserved for more than one month did not degrade. The weak spectral features that appear as shoulders at 547 and 593 nm in the extinction spectrum of the $[r_1, r_2] = [90, 120]$ nm quadrupolar nanoshell/J-aggregate complex (Fig. 4.2c black curve) are attributable to residual dye monomers that remain in solution.

Surface enhanced Raman scattering (SERS) measurements were also performed to confirm the formation of the nanoshell/J-aggregate complex (Fig. 4.3). Nanoshells

were first immobilized onto cleaned quartz substrates using a 0.1 % by weight polyvinyl pyridine solution in ethanol, a procedure shown previously to yield well-dispersed single nanoshells on a variety of substrate surfaces. Complex formation was performed by immersion of these nanoshell-coated quartz slides into 0.5 mM dye solution for several hours. Before acquiring Raman spectra, the sample was rinsed several times with water. SERS spectra were obtained using a Renishaw inVia Raman microscope (Renishaw, United Kingdom) with 785 nm wavelength excitation, 55 μ W laser power at the sample, a 63X water immersion lens (Leica, Germany) for light collection, and a 30 s integration time. Fig. 4.3 shows the experimental (a) SERS spectra of the 2,2'-dimethyl-8-phenyl-5,6,5',6',-dibenzothiacarbocyanine chloride complexed with the nanoshells, compared with (b) normal Raman spectra of the same molecule in solution (normal Raman spectra of the isolated molecule and its J-aggregate in solution were found to be virtually indistinguishable). The strong SERS spectra directly confirm that the molecular J-aggregates remain bound to the nanoshell surface even after rinsing.

4.4 Results and Discussion

In the nanoshell/J-aggregate complexes, the plasmons interact with excitons giving rise to plasmon/exciton mixed states. This process can be described as a hybridization between the plasmons and excitons of the complex.[1, 111] Plasmon hybridization theory, which has been developed for the plasmon response of complex

nanostuctures,[1] can be extended to describe the interaction between nanoshell plasmons and J-aggregate excitons to describe this type of complex. In Fig. 4.2b,c, the peaks at low energy represent the bonding states (with the plasmonic and excitonic excitations in phase with each other) while those at high energy represent the anti-bonding states (when the plasmonic and excitonic excitations are out of phase). The fact that the two peaks in the spectra of Fig. 4.2b,c are of almost equal intensity implies that the excitons and localized plasmons are in their strongest interaction regime. This is when the exciton resonance energy corresponds to the peak dipole or quadrupole plasmon resonance energy.

To determine the coherent coupling energy for the localized plasmon/exciton system, dispersion curves were obtained for the nanoshell/J-aggregate complexes. This was done by tuning the nanoshell plasmon resonance energy across the J-aggregate absorption band by varying the nanoshell core size/shell thickness (r_1/r_2) ratio. Nanoshells of dimensions $[r_1, r_2] = [40, 58]$ nm, $[40, 55]$ nm, $[45, 63]$ nm, $[45, 60]$ nm, $[45, 54]$ nm, and $[60, 83]$ nm were used to obtain data points for the dipole dispersion curve (Fig. 4.4); while $[r_1, r_2] = [90, 127]$ nm, $[90, 123]$ nm, $[90, 120]$ nm, $[90, 115]$ nm, $[90, 110]$ nm, and $[90, 107]$ nm were used to obtain the data points for the quadrupole dispersion curve (Fig. 5). The order in which the nanoshell dimensions are listed corresponds to data points in each respective dispersion curve. The experimental extinction spectra of the pristine nanoshells in water are shown in

Fig. 4.4a and 4.5a, while those of the nanoshell/J-aggregate complexes are shown in Fig. 4c and 5c. The number of nanoshells per milliliter of H₂O was approximately 6.68×10^9 for dipole samples and 1.86×10^9 for quadrupole samples. Twelve microliters of the dye solution was added to 3.5 mL of aqueous solution for each of the nanoshell solutions. Extinction spectra of all samples were obtained directly following the formation of the nanoshell/J-aggregate complexes. Peak energies of the resulting "plexcitonic" complexes were then plotted as a function of the plasmon energy of the pristine nanoparticles.

In the dispersion curves shown in Fig. 4.4e and 4.5e, the low energy plasmon/exciton energy is shown in blue and the high energy plasmon/exciton peak is shown in red. Uncoupled plasmon and exciton energies are represented by the green and black lines, respectively. The dispersion curves display an avoided crossing at the energy position where the uncoupled plasmon and exciton energies overlap. The splitting energy corresponds to the coupling strength between plasmons and excitons. The coupling energy from the dipole plasmon dispersion curve is approximately 120 meV while that from the quadrupole dispersion curve is less, approximately 100 meV.

From our analysis, it appears that the observed splitting energies for our nanoshell/J-aggregate complexes are limited by the thickness of the J-aggregate layer on the nanoparticle surface. On the basis of the molecular absorbance of the dye molecules and nanoshells used in this experiment, we estimate that the "effective" thickness,

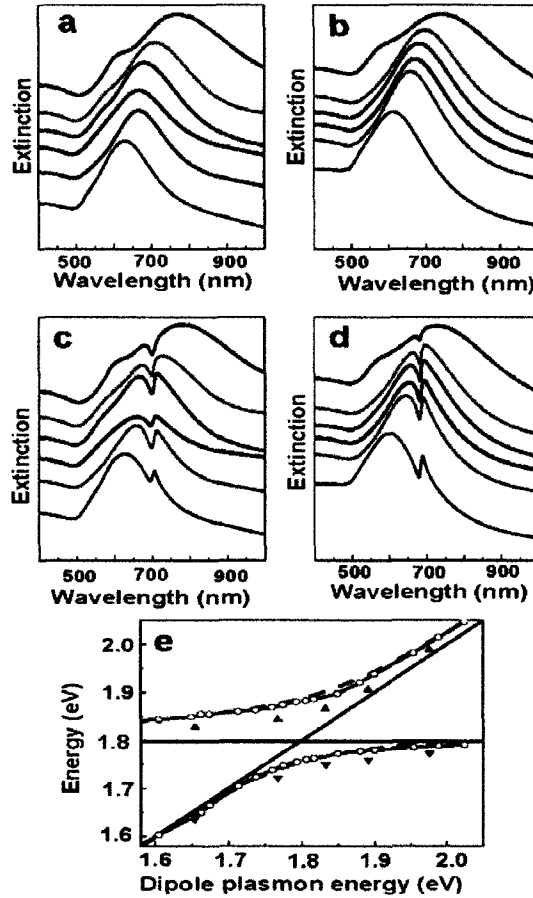


Figure 4.4 (a) Experimental extinction spectra of aqueous gold nanoshell solution showing dipole plasmon tuning. Nanoshell sizes from top to bottom are $[r_1, r_2] = [60, 83]$ nm, $[45, 54]$ nm, $[45, 60]$ nm, $[45, 63]$ nm, $[40, 55]$ nm, and $[40, 58]$ nm. (b) Gold nanoshell extinction spectra obtained from Mie scattering theory. (c) Experimental extinction spectra of aqueous solution of gold nanoshell/J-aggregate complexes. (d) Theoretical extinction spectra of gold nanoshell/J-aggregate complex obtained from Mie calculations. Johnson and Christy parameters are used for the Au shell and $\epsilon_1 = 2.04$ for the silica core. $\epsilon_{\infty J} = 1$, $f = 0.02$, and $\gamma \sim 0.052$ for the J-aggregate molecular layer. (e) Dispersion curve from experimental data (diamond), Mie scattering theory (circle dashed line), and Gans theory (dashed line). The black and green lines represent uncoupled exciton and plasmon energies. Blue and red colors represent low and high energy plasmon-exciton hybrid states, respectively.

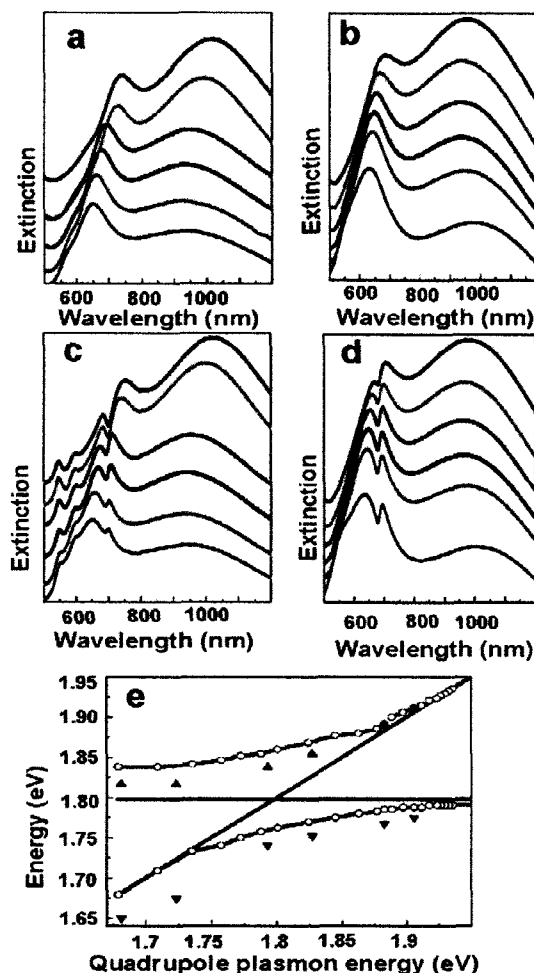


Figure 4.5 (a) Experimental extinction spectra of aqueous gold nanoshell solution showing quadrupole plasmon tuning. Nanoshell sizes from top to bottom are $[r_1, r_2] = [90, 107]$ nm, $[90, 110]$ nm, $[90, 115]$ nm, $[90, 120]$ nm, $[90, 123]$ nm, and $[90, 127]$ nm. (b) Gold nanoshell extinction spectra obtained from Mie scattering theory. (c) Experimental extinction spectra of aqueous solution of gold nanoshell/J-aggregate complexes. (d) Theoretical extinction spectra of gold nanoshell/J-aggregate complex obtained from Mie calculations. Johnson and Christy parameters are used for the Au shell and $\epsilon_1 = 2.04$ for the silica core. $\epsilon_{\infty J} = 1$, $f = 0.02$, and $\gamma \sim 0.052$ for the J-aggregate molecular layer. (e) Dispersion curve from experimental data (diamond) and Mie scattering theory (circle dashed line). The black and green lines represent uncoupled exciton and plasmon energies. Blue and red colors represent low and high energy plasmon-exciton hybrid states, respectively.

or the depth of J-aggregate coupled to the nanoshell plasmon, is nominally 4 nm. In an attempt to increase the splitting energy of the nanoshell/J-aggregate complex, nanoshells were first functionalized with sodium 2-mercaptoethanesulfonate prior to complexation with J-aggregates, to increase the negative charge on the nanoshell surface relative to complex formation with pristine nanoshells. The prefunctionalized sulfonated nanoshells were then exposed to dye solutions of various concentrations to produce J-aggregates of various molecular coating thicknesses. The splitting energies of these complexes as a function of the dye concentration used in formation of the nanoshell/J-aggregate complexes are shown in Fig. 4.6. While any further increase in splitting using this approach is rather small, indicating that the effective thickness may already have been reached, this experiment reveals a strong asymmetry in the onset of plasmon/exciton interaction in this complex, an effect that may be related to dielectric screening or phase retardation effects.[112]

4.5 Conclusion

We have shown that the coherent coupling between the plasmons of the nanoshell particle and the excitons of the J-aggregate can create the new hybridized state, using classical electromagnetic theory. The theoretical calculations of optical absorption for nanoshell/J-aggregate complexes could explain the experimental results of the extinction spectra. Strongly asymmetric splitting energies as large as 120 meV are observable in these complexes, where the splitting energy depends upon the plasmon

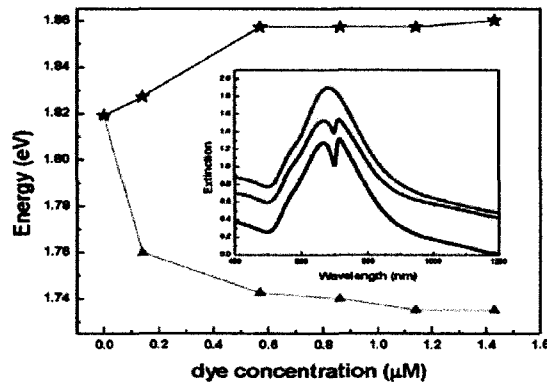


Figure 4.6 Onset of splitting in plasmon/J-aggregate complex as a function of dye concentration in media, which controls deposition of the J-aggregate adlayer on the nanoshell surface. Inset: nanoshell/J-aggregate plexciton spectra for various dye concentrations shown: 0 μL (red), 4 μL (blue), 10 μL (black). Spectra shown are offset for clarity.

mode of the complex. We believe that this result may stimulate interest in the fabrication and properties of coupled plasmon/exciton nanostructures with controlled coupling, and with optical properties unique to this new class of nanoparticle-based materials.

Chapter 5

Plasmonic Properties of a Metallic Torus

5.1 Introduction

The electronic and optical properties of nanoparticles are topics of considerable current interest in nanoscience.[113, 114, 115] Novel nanofabrication and templating techniques are making it possible to fabricate metallic nanostructures of complex shapes and with unusual properties.[116, 117, 118, 119, 120, 121] The optical properties of metallic nanostructures are determined by their plasmon resonances which can depend sensitively on their shape, composition, and dielectric environment.[122, 123, 2, 81, 124, 125, 126, 127] For certain nanoparticles such as nanoshells[128] and nanorods,[129] the plasmon energies can be tuned all the way from the visible part of the spectrum well into the mid-infrared. This tunability has been exploited in a variety of important applications such as chemical and biological sensing,[5] optical manipulation of nanoparticles,[130] plasmonic waveguiding,[131, 132] metamaterials,[55, 133] and biomedical applications.[134, 135, 136]

The metallic nanoring or nanotorus is an interesting highly tunable plasmonic geometry with significant potential as a substrate for chemical and biological sensing, and possible magnetic effects at optical frequencies.[137, 138, 139, 69] The optical properties of nanorings have been calculated using the boundary element method,[140, 141] and the dyadic Green's tensor approach.[142, 143] and the Finite difference Time

Domain (FDTD) method.[144]

In this work, we investigate the plasmonic and optical properties of metallic tori using the Plasmon Hybridization (PH) method.[1, 16] We show that the plasmon resonances in a nanotorus results from hybridization of primitive plasmon modes that can be described as toroidal harmonics. The energies of the hybridized plasmon modes depend on the aspect ratio of the torus which we define as the ratio of the radius of the tube r to the radius of the ring R , $X = \frac{r}{R}$. The plasmonic structure and optical absorption spectrum are found to be strongly dependent on the polarization. For polarization parallel to the ring, two distinct features appear in the absorption spectrum: a low intensity, high energy feature corresponding to the excitation of several higher order overlapping torus modes and a stronger low energy feature corresponding to a dipolar plasmon oscillation in the plane of the ring. The energy of this resonance is strongly dependent on the aspect ratio of the torus. For aspect ratios smaller than $X=0.8$, we show that the dipolar mode can be described analytically as an infinite cylinder plasmon of a wavelength equal to the circumference of the torus, $2\pi R$. For light polarized perpendicular to the ring, the spectra displays two very closely spaced modes which can be interpreted as the bonding and antibonding combinations of two infinite cylinder plasmons of different azimuthal symmetry. The energies of these modes are only very weakly dependent on the aspect ratio of the ring.

The paper is organized as follows. In section 5.2 we present the extension of the

PH method to particles that can be described in toroidal coordinates. In section 5.3, we compare the results of the PH method with FDTD. We examine the effect of retardation and present calculations of the local electric field enhancements.

5.2 Theory

The PH method has recently been reviewed with several relevant applications and will only be discussed briefly here.[59] In short, it is an exact electrostatic approach where the plasmons are considered as incompressible deformations of the conduction electron liquid of a uniform density n_0 with respect to an oppositely charged background. The deformation field of the conduction electron liquid is expanded in a complete basis (primitive plasmons) which interact with each other through their surface charges. These interactions results in hybridized plasmon modes that can be expressed as linear combinations of the primitive plasmon modes. These hybridized plasmon modes constitute the plasmonic eigenmodes of the system. Since the kinetic energy of the deformation field is explicitly accounted for, the Drude contribution to the dielectric response is implicit in the method. To account for the dielectric screening contributed from the ionic backgrounds of the metals or from solvents, only the Coulomb interaction between the primitive plasmons is modified. The PH method provides a fast and intuitive description of the plasmon modes of a complex nanostructure. When compared to fully retarded approaches,[145, 146] the method has been shown to be accurate for nanostructures of physical extents smaller than around

a quarter of the wavelength of the incident light.

5.2.1 Plasmonic structure

All physical quantities required for the description of the plasmons can be expressed in terms of a hydrodynamic scalar potential $\eta(\vec{r}, t)$ which satisfies the Laplace equation,[16]

$$\nabla^2 \eta = 0. \quad (5.1)$$

The spill-out surface charge density σ is given by

$$\dot{\sigma}(t) = n_0 e \frac{\partial \eta}{\partial \hat{n}}, \quad (5.2)$$

where n_0 and e are the number of electrons per unit volume of the metal, and the electron charge, respectively. \hat{n} is the outward unit vector normal to the surface. The dot above σ indicates the time-derivative. The kinetic energy, T , is given by

$$T = \frac{n_0 m_e}{2} \int \eta \vec{\nabla} \eta \cdot d\vec{S}, \quad (5.3)$$

where $d\vec{S}$ is the surface element and m_e the effective mass of a conduction electron.

The nonretarded Coulomb interaction energy V , is given by

$$V = \frac{1}{2} \int \frac{\sigma(\vec{r}) \sigma(\vec{r}')}{|\vec{r} - \vec{r}'|} dS_{\vec{r}} dS_{\vec{r}'}. \quad (5.4)$$

In a recent paper we generalized the PH method to nanostructures with a geometry that can be expressed in separable curvilinear coordinates.[50] In toroidal coordinates

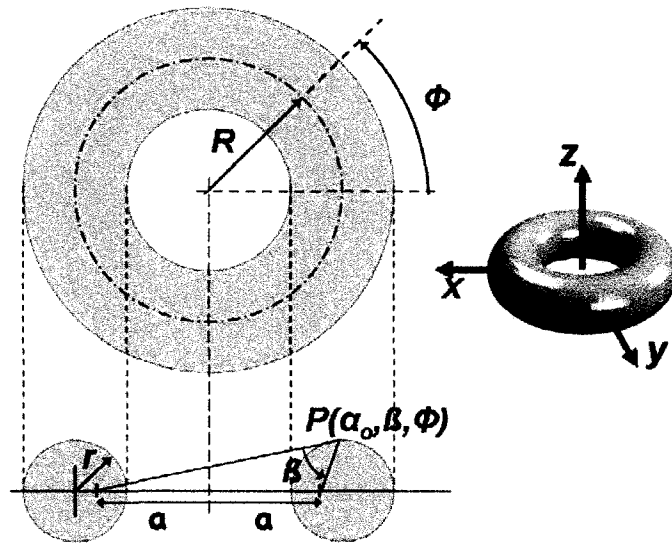


Figure 5.1 A schematic diagram of a torus and the toroidal angular coordinates. The origin of the Cartesian coordinates is at the center of the symmetry, and the z -axis is normal to the toroidal plane. R and r are the major and minor radii of the torus, respectively. The surface of the torus is defined by $\alpha = \alpha_0$ (Eq. 5.11). For a point P on the surface of the torus, the offset parameter $a = r \sinh \alpha_0$. As $r \rightarrow 0$, $a \rightarrow R$ and the angular coordinate β becomes equivalent to the azimuthal angle in a cylinder.

as illustrated in Fig. 1, (α, β, ϕ) (following the notation of [147]), the general solution to Eq. (5.1) is not completely separable but takes the form

$$\eta(\alpha, \beta, \phi; t) = \sum_{\mu} \sum_{\nu} \dot{G}_{\mu, \nu}(t) \eta_{\mu, \nu}(\alpha, \beta, \phi) \quad (5.5)$$

where $\dot{G}_{\mu, \nu}(t)$ is the time-derivative of the primitive plasmon amplitude and the basis functions $\{\eta_{\mu, \nu}(\alpha, \beta, \phi)\}$ are the scalar functions for the corresponding primitive plasmons. In toroidal symmetry, the primitive plasmons are labeled by the indexes (μ, ν) . The index μ is similar to the multipolar index m that is commonly used in spherical or cylindrical symmetry. As will be demonstrated below, primitive plasmons of different μ will not interact and the allowed values for ν is zero and positive integers. In the calculations, the summation over ν will be truncated at a maximum value ν_{max} which depends on the geometry of the torus.

The primitive plasmons $\eta_{\mu, \nu}(\alpha, \beta, \phi)$ have the form,

$$\eta_{\mu, \nu}(\alpha, \beta, \phi) = \sqrt{D(\alpha, \beta)} A_{\mu, \nu}(\alpha) B_{\nu}(\beta) \Phi_{\mu}(\phi) \quad (5.6)$$

where

$$D(\alpha, \beta) = \cosh \alpha - \cos \beta. \quad (5.7)$$

Substituting Eq. (5.6) in Eq. (5.1), we obtain the following set of second order differential equations.

$$\frac{d^2 \Phi(\phi)}{d\phi^2} + \mu^2 \Phi(\phi) = 0 \quad (5.8)$$

$$\frac{d^2 B(\beta)}{d\beta^2} + \nu^2 B(\beta) = 0 \quad (5.9)$$

$$\frac{1}{\sinh \alpha} \frac{d}{d\alpha} \left(\sinh \alpha \frac{dA_{\mu,\nu}(\alpha)}{d\alpha} \right) - \left(\nu^2 - \frac{1}{4} + \frac{\mu^2}{\sinh^2 \alpha} \right) A_{\mu,\nu}(\alpha) = 0 \quad (5.10)$$

The two linearly independent solutions of each of Eq. (5.8), (5.9), and (5.10) are, $\Phi(\phi) = \{\cos \mu\phi, \sin \mu\phi\}$, $B(\beta) = \{\cos \nu\beta, \sin \nu\beta\}$, and $A_{\mu,\nu}(\alpha) = \{P_{\nu-\frac{1}{2}}^\mu(\cosh \alpha), Q_{\nu-\frac{1}{2}}^\mu(\cosh \alpha)\}$, respectively. The functions $P_{\nu-\frac{1}{2}}^\mu$ and $Q_{\nu-\frac{1}{2}}^\mu$ are the first and second modified Legendre functions respectively. The ranges of the spatial variables, α, β , and ϕ , are $\alpha \in (0, \infty)$, $\beta \in (-\pi, +\pi)$, and $\phi \in (-\pi, +\pi)$. The solutions must be periodic in ϕ and β . Therefore, μ and ν are zero or positive integers. Because of the symmetry of toroid, a rotation of the x and y -axes around the z -axis (see Fig. 5.1) by $\pi/2$ does not change the physical conditions, and $\cos \mu\phi$ in the old axes is equivalent to $\sin \mu\phi$ in the new rotated axes. Therefore, in the following we will use only $\Phi_\mu(\phi) = \cos \mu\phi$.

The surface of the torus is defined by $\alpha = \alpha_0$ given by

$$\cosh \alpha_0 = \frac{R}{r} \equiv \frac{1}{X} \quad (5.11)$$

where R and r are the major radius and the minor radius of a toroid (See Fig. 5.1) and X is the aspect ratio of the torus. The internal (external) space of the toroid is given by $\alpha > \alpha_0$ ($\alpha < \alpha_0$). Since the electron fluid is confined in the internal space of the toroid, the space of our interest is $\alpha > \alpha_0$. The values and gradients of $P_{\nu-\frac{1}{2}}^\mu(\cosh \alpha)$

are singular at $r=0$. Therefore, the $P_{\nu-\frac{1}{2}}^\mu(\cosh \alpha)$ term does not correspond to physical charge deformations and should be omitted. The primitive plasmons thus take the form,

$$\eta_{\mu,\nu,i}(\alpha, \beta, \phi) = \sqrt{D(\alpha, \beta)} Q_{\nu-\frac{1}{2}}^\mu(\cosh \alpha) B_\nu^i(\beta) \cos \mu \phi, \quad (5.12)$$

where the index i denotes the $\cos \nu \beta$ or the $\sin \nu \beta$ solution for $B_\nu(\beta)$ in Eq. (5.9) and will be referred to as “cosine” and “sine” modes respectively.

Since both the kinetic and potential energies Eqs. (5.3) and (5.4) involve only surface integrals, η and $\vec{\nabla} \eta$ are evaluated at $\alpha = \alpha_0$. The surface element is given by

$$d\vec{S} = \hat{n} \frac{C^2 \sinh \alpha_0}{D^2(\alpha_0, \beta)} d\beta d\phi, \quad (5.13)$$

where the scale factor is defined as $C = \sqrt{R^2 - r^2}$. The component of $\vec{\nabla} \eta_{\mu,\nu,i}$ normal to the surface element is

$$\vec{\nabla} \eta_\perp = -\hat{n} \left[\frac{D(\alpha, \beta)}{C} \frac{\partial \eta_{\mu,\nu,i}}{\partial \alpha} \right]_{\alpha=\alpha_0}, \quad (5.14)$$

where

$$\begin{aligned} \left[\frac{\partial \eta_{\mu,\nu,i}}{\partial \alpha} \right]_{\alpha=\alpha_0} &= \left[\frac{a_{\mu,\nu}^{(1)}}{\sqrt{D(\alpha_0, \beta)}} + a_{\mu,\nu}^{(2)} \sqrt{D(\alpha_0, \beta)} \right] \\ &\quad \times B_\nu^i(\beta) \cos \mu \phi, \end{aligned} \quad (5.15)$$

and

$$a_{\mu,\nu}^{(1)} = \frac{1}{2} \sinh \alpha_0 Q_{\nu-\frac{1}{2}}^\mu(\cosh \alpha_0) \quad (5.16)$$

$$a_{\mu,\nu}^{(2)} = \left[\frac{dQ_{\nu-\frac{1}{2}}^\mu(\cosh \alpha)}{d\alpha} \right]_{\alpha=\alpha_0}. \quad (5.17)$$

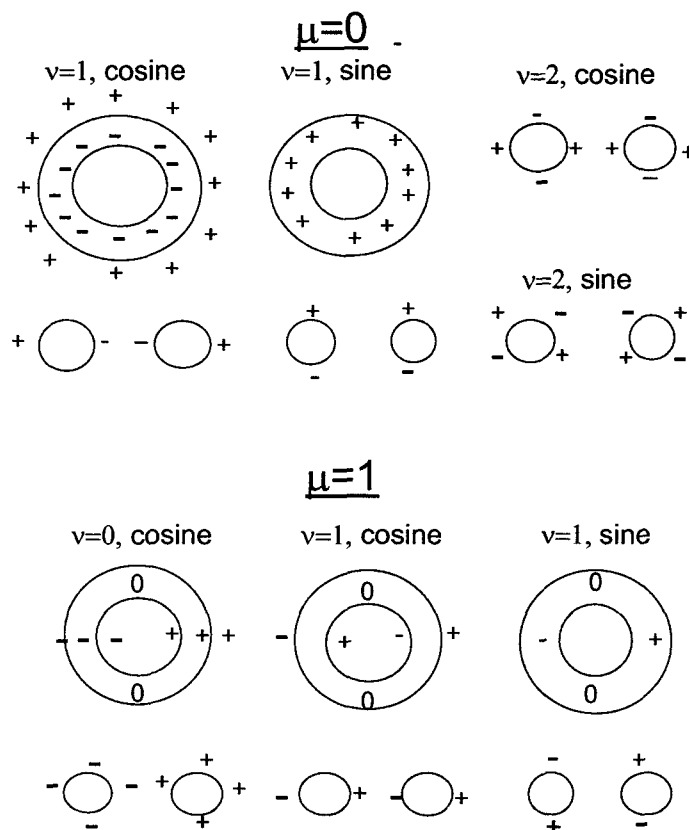


Figure 5.2 Schematic illustration of the top and side views of the surface charge distribution induced by several of the lowest order primitive plasmon modes for a torus of small aspect ratio X .

The derivatives of the modified Legendre functions can be expressed in terms of lower order functions.[148]

The surface charge induced by a primitive plasmon mode is obtained from the time-integration of the normal derivative of the corresponding scalar potential Eq. (5.2) at the surface α_0 of the torus. In Fig. 5.2 we schematically illustrate the surface charge distribution associated with the lowest order primitive plasmon modes. The index μ

refers to the ϕ variations, and the ν index denotes the β variation. For $\mu = 0$, the surface charges does not depend on the angle ϕ , and there is no $\nu = 0$ mode since this mode is a compressible deformation. For $\mu = 1$ the surface charges are of opposite signs across the torus.

The matrix elements of the kinetic energy Eq. (5.3) contain the definite integral,

$$I_\phi(\mu, \mu') = \int_{-\pi}^{\pi} \cos \mu \phi \cos \mu' \phi d\phi = \pi(1 + \delta_{\mu,0})\delta_{\mu,\mu'}. \quad (5.18)$$

where $\delta_{\mu,\mu'}$ is the Kronecker delta function. Since a nonvanishing matrix element is only obtained for $\mu = \mu'$, the kinetic energy matrix element can be written as,

$$\begin{aligned} T_{\nu,i,\nu',i'}^\mu &= C_T^\mu \dot{G}_{\mu,\nu,i}(t) \dot{G}_{\mu,\nu',i'}(t) Q_{\nu-\frac{1}{2}}^\mu (\cosh \alpha_0) \\ &\times \int_{-\pi}^{\pi} \left[\frac{a_{\mu,\nu'}^{(1)}}{D(\alpha_0, \beta)} + a_{\mu,\nu'}^{(2)} \right] B_\nu^i(\beta) B_{\nu'}^{i'}(\beta) d\beta \end{aligned} \quad (5.19)$$

where C_T^μ is a constant coefficient defined as

$$C_T^\mu = \frac{n_0 m_e C \sinh \alpha_0 I_\phi(\mu, \mu)}{2} \quad (5.20)$$

The calculation of the potential energy matrix element Eq. (5.4) can be simplified by expanding the Coulomb potential in toroidal coordinates[149],

$$\begin{aligned} \frac{1}{|\vec{r} - \vec{r}'|} &= \frac{1}{C\pi} \sqrt{D(\alpha_0, \beta) D(\alpha_0, \beta')} \sum_{n=0}^{\infty} \sum_{m=0}^{\infty} \epsilon_n \epsilon_m (-1)^m \frac{\Gamma(n - m + \frac{1}{2})}{\Gamma(n + m + \frac{1}{2})} \\ &\times Q_{n-\frac{1}{2}}^m(\cosh \alpha_0) P_{n-\frac{1}{2}}^m(\cosh \alpha_0) \cos m(\phi - \phi') \cos n(\beta - \beta'), \end{aligned} \quad (5.21)$$

where the points \vec{r} and \vec{r}' lie on the surface of the torus $\alpha = \alpha_0$. In this expression ϵ_k is the so-called Neumann factor,[149] which is equal to 1 if $k = 0$ and 2 if $k \geq 1$. Then,

substituting Eq. (5.21) in Eq. (5.4) and carrying out the ϕ and ϕ' integrations, we again obtain finite contributions only for $\mu = \mu' = m$. The potential energy matrix element can thus be written as

$$\begin{aligned}
V_{\nu,i,\nu',i'}^{\mu} = & \left[\frac{1}{2\pi} (n_0 e)^2 I_{\phi}^2(\mu, \mu) C \sinh^2 \alpha_0 \right] \epsilon_{\mu} (-1)^{\mu} \sum_{n=0}^{n_{max}} \epsilon_n \frac{\Gamma(n - \mu + \frac{1}{2})}{\Gamma(n + \mu + \frac{1}{2})} \\
& \times Q_{\nu-\frac{1}{2}}^{\mu}(\cosh \alpha_0) P_{\nu-\frac{1}{2}}^{\mu}(\cosh \alpha_0) \int_{-\pi}^{\pi} d\beta \int_{-\pi}^{\pi} d\beta' \left[\frac{a_{\mu,\nu}^{(1)}}{D(\alpha_0, \beta)} + a_{\mu,\nu}^{(2)} \right] \\
& \times \left[\frac{a_{\mu,\nu'}^{(1)}}{D(\alpha_0, \beta')} + a_{\mu,\nu'}^{(2)} \right] \cos n(\beta - \beta') B_{\nu}^i(\beta) B_{\nu'}^{i'}(\beta') G_{\mu,\nu,i}(t) G_{\mu,\nu',i'}(t).
\end{aligned} \tag{5.22}$$

The required n_{max} for convergence in Eq. (5.21) increases with increasing aspect ratio X , and depends on ν and ν' . We found that an $n_{max} = \nu_{max} + 3$ where ν_{max} is the largest ν included in the summation Eq. (5.5) was sufficient for the largest X investigated in this study.

The integrals over the angles β and β' in Eqs. (5.19) and (5.22) involve products of B_{ν}^i and $B_{\nu'}^{i'}$ functions and are zero for cosine-sine combinations ($i \neq i'$). Thus both the kinetic energy and the potential energy matrices are diagonal in μ and i and the Lagrangian $L = \sum_{\mu,i} L^{\mu,i}$ can be solved for fixed μ and i . In the equation of motion, we renormalize the kinetic and potential energy matrices to $\hat{T}^{\mu,i}$ and $\hat{V}^{\mu,i}$ by dividing with C_T^{μ} Eq. (5.20) and use the bulk plasmon frequency,

$$\omega_B = \sqrt{\frac{4\pi e^2 n_0}{m_e}} \tag{5.23}$$

to eliminate n_0 , e , and m_e . The plasmon frequencies of symmetry μ and i of the torus are then given by the solutions to

$$\det \left[\omega^2 \hat{T}^{\mu,i} - \frac{\omega_B^2 \sinh \alpha_0 (1 + \delta_{\mu,0})}{4\pi} \hat{V}^{\mu,i} \right] = 0. \quad (5.24)$$

We notice that Eq. (5.24) does not involve the scale factor C , and depends only on α_0 of Eq. (5.11). Therefore, the eigenmodes ω depend only on the aspect ratio X and not on the physical size of the toroid as expected in the electrostatic limit.[16]

5.2.2 Optical absorption

To calculate the optical absorption, the coupling between the primitive plasmon modes and the incident light needs to be added to the Lagrangian of the system. In the electrostatic limit the incident light interacts with the primitive plasmons only through their dipole moments. Due to the angular symmetry of the torus, we will only consider the dipolar interactions for light polarizations in the parallel (\hat{x}) and perpendicular (\hat{z}) directions. The Cartesian coordinates x and z can be expressed in the toroidal coordinates as,

$$x = C \sinh \alpha_0 \frac{\cos \phi}{D(\alpha_0, \beta)}, \quad z = C \frac{\sin \beta}{D(\alpha_0, \beta)} \quad (5.25)$$

The dipolar couplings for \hat{x} and \hat{z} polarization can be written

$$V_{x,z}^{\mu,\nu,i} = G_{\mu,\nu,i}(t) d_{x,z}^{\mu,\nu,i} \quad (5.26)$$

where

$$d_{x,z}^{\mu,\nu,i} = \int \{x, z\} \sigma_{\mu,\nu,i} dS. \quad (5.27)$$

For parallel polarization, the incident field only couples to $\mu=1$ cosine plasmons and for perpendicular polarization, only to $\mu=0$ sine plasmons. For a finite aspect ratio X , an incident dipolar field can couple to all primitive ν modes. However as can be seen from the schematic diagram of the surface charge distributions in Fig. 2, sizable couplings will only be present for the lowest ν . For parallel polarization, the dominant couplings are to the $\mu=1, \nu=0$ and $\mu=1, \nu=1$ cosine modes. The magnitude of the $\nu = 1$ coupling is smaller than the coupling to the $\nu=0$ mode by a factor approximately equal to the aspect ratio X . For perpendicular polarization, only the primitive $\mu=0, \nu=1$ sine mode couples significantly to an incident dipolar field. However, for both parallel and perpendicular polarization, due to the interactions, all hybridized modes will contain dipole-active primitive plasmons and can be excited by dipolar field.

With the coupling to the incident light included in the Lagrangian, the equations of motion take the form,

$$\left[\omega^2 \hat{T}^{\mu,i} - \frac{\omega_B^2 \sinh \alpha_0 (1 + \delta_{\mu,0})}{4\pi} \hat{V}^{\mu,i} \right] \vec{G}^{\mu,i} = \frac{1}{C_T^\mu} \vec{d}^{\mu,i} \quad (5.28)$$

where $\vec{G}^{\mu,i} = \{G_{\mu,\nu,i}(t)\}_\nu$ is the primitive plasmon amplitude vector, and $\vec{d}^{\mu,i}$ is a vector $\{d_{x,z}^{\mu,\nu,i}\}_\nu$ where $\mu=1$ and i refers to cosine modes for parallel (\hat{x}) polarization and $\mu=0$ and i refers to sine modes for perpendicular (\hat{z}) polarization. This equation gives the plasmon amplitudes, \vec{G} , in the presence of the incident light. From these primitive plasmon amplitudes, the induced dipole moment (dipolar polarizability $\alpha(\omega)$) is calculated. The absorption cross section, $\sigma_{abs}(\omega)$ is obtained from the

imaginary part of the complex frequency dependent dipolar polarizability,[16]

$$\sigma_{abs}(\omega) = \frac{\omega}{c} \text{Im}[\alpha(\omega + i\delta)] \quad (5.29)$$

In the above c is the speed of light, and δ is the damping. The product $\delta\omega$ gives the HWHM of the spectral lines.[50] In a realistic calculation δ should be determined from the imaginary part of the dielectric function and will in general be frequency dependent.[20]

5.3 Results

The required number of coupled primitive modes ν_{max} for convergence increases with the aspect ratio of the torus. For aspect ratios close to 1, the two inner surfaces of the torus lie very close to each other enabling a strong interaction and hybridization of primitive plasmon modes with different ν . Since our approach is variational, the energy of the lowest mode will decrease monotonously with increasing ν_{max} . For the aspect ratios considered in this paper we found that $\nu_{max}=35$ was sufficient. To evaluate the toroidal Legendre functions we use public domain software.[150] To model gold metal we neglect the dielectric background screening mediated by the gold ions and use a renormalized bulk plasmon frequency $\omega_B=4.6$ eV. This choice of dielectric parameters places the dipolar resonance of a solid sphere at 2.6 eV in agreement with experimental data and provides a reasonable description of the plasmonic interactions in general nanoparticles. For the damping parameter δ we will use sufficiently small

values that individual plasmonic modes of the torus can be resolved. The extension to a more realistic dielectric background screening is straightforward but would significantly complicate the theoretical formalism.[20]

5.3.1 Plasmonic structure

In Fig. 5.3, we show several of the lowest energy $\mu=1$ hybridized cosine modes as functions of the aspect ratio, X . The energy of the lowest mode shows a strong aspect ratio dependence and increases from zero to a maximum value at $0.45\omega_B$ for $X \sim 0.94$. For larger X , the energy decreases due to the strong interaction of the surface charges on the interior surfaces of the torus. The second-lowest energy mode exhibits a relatively weak dependence on aspect ratio with a minimum around $X=0.85$ and a slight blueshift for aspect ratios close to 1. The higher energy modes are clustered together around $0.7\omega_B$ and do not depend sensitively on the aspect ratio. The two lowest energy hybridized torus modes are both dipole active and their energies can be extracted from their corresponding peak positions in FDTD spectra. The figure shows the FDTD result obtained for small tori and a Drude dielectric function. The tori are chosen sufficiently small that retardation effects are negligible. The small deviations between the FDTD and PH results are caused by numerical stair-casing effects in the FDTD simulations.[146]

The results in Fig. 5.3 are in excellent agreement with the results by Mary et al.[142] who calculated the plasmon energies of a torus using an electrostatic dyadic

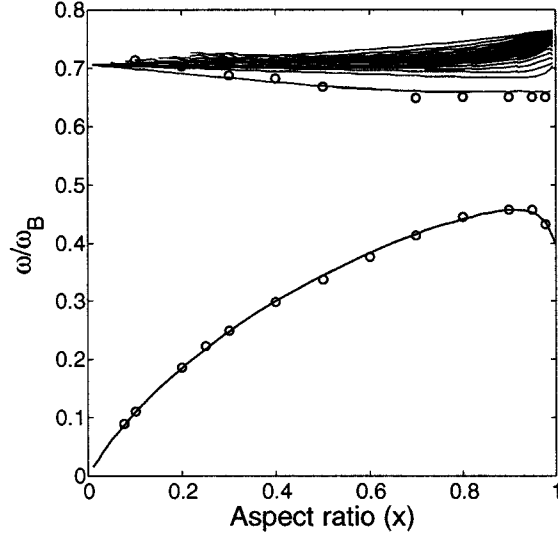


Figure 5.3 The solid lines are the hybridized $\mu = 1$ cosine plasmon energy levels of a metallic torus as a function of the aspect ratio X calculated using the PH method. The open circles are the results for the lowest energy plasmon modes obtained from FDTD simulations for very small tori ($R < 25$ nm).

Green's tensor approach. Their definition of the aspect ratio, x_m , is different from our X and related as $X = x_m/(2 + x_m)$.

Figure 5.4 shows the plasmon energies versus aspect ratio for several different ν_{max} and illustrates the nature of the plasmon hybridization resulting in the formation of two lowest hybridized modes in Fig. 3. The figure shows that the magnitude of the hybridization of the primitive torus modes depends on the aspect ratio of the structure. For a thin torus, $X < 0.1$, since there is only little change of the plasmon energy when adding more primitive modes, the effect of hybridization is minimal. The two plasmon modes are essentially pure primitive $\nu=0$ and $\nu=1$ torus plasmons. As the aspect ratio is increased these two primitive modes begin to interact forming a

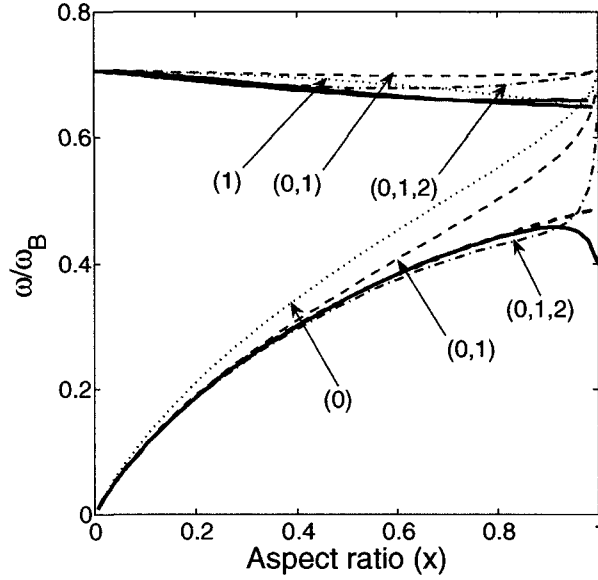


Figure 5.4 Plasmon hybridization in a torus for parallel polarization, i.e., $\mu = 1$ cosine modes. The black solid lines are the energies of the two lowest modes for $\nu_{max} = 1$ (dashed), 2 (dot-dashed), and 35 (solid). The lower dotted line is the energy of the individual $\nu = 0$ primitive plasmon and the upper dotted line is the energy of the individual $\nu = 1$ mode. The red lines are the analytical infinite cylinder result Eq. (5.30) for $k = 1/R$ and $m' = 0$ (dashed) and $m' = 1$ (solid).

bonding hybridized $\nu=0$ mode and an antibonding hybridized $\nu=1$ mode. For aspect ratios $0.1 < X < 0.4$ the bonding mode is well described by only including the $\nu=1$ mode in the basis set. For aspect ratios $0.4 < X < 0.8$ it is necessary to also include the primitive $\nu=2$ mode in the basis set.

For the antibonding $\nu=1$ mode, we note that for aspect ratios $X > 0.2$, the hybridization with the lower energy $\nu=0$ mode results in a too large blueshift. Including the higher energy primitive $\nu=2$ mode is sufficient for aspect ratios up to $X=0.4$. For a satisfactory description of the higher energy mode for $X > 0.4$, higher

order primitive plasmons $\nu > 2$ are necessary.

For a thin torus, the local geometric structure resembles that of a solid cylinder and one could envision describing the torus modes as standing cylinder plasmons of wavelengths determined by the circumference of the torus. It is therefore of interest to investigate the relations between plasmons in a torus and those of a metallic cylinder. In the absence of dielectric backgrounds, the plasmon resonances for an infinite cylinder of radius r are,[21]

$$\omega_{m'} = \omega_B \sqrt{kr I'_{m'}(kr) K_{m'}(kr)}. \quad (5.30)$$

In this expression $I_{m'}$ and $K_{m'}$ are modified Bessel functions of order m' . The quantity m' refers to the azimuthal symmetry of the plasmon modes of a cylinder and k is the wavevector in the direction of the cylinder axis. For a thin torus, the β coordinate is equivalent to the azimuthal cylinder coordinate ϕ . The $\mu=1$ modes correspond to cylinder plasmons of a wavelength equal to the circumference of the torus $2\pi R$, i.e. with $k = 1/R$. The lowest energy cylinder plasmon is obtained for $m'=0$ which corresponds to a primitive $\mu=1, \nu=0$ cosine plasmon in a thin torus. The second lowest energy cylinder plasmon for $k = 1/R$ is the $m'=1$ mode. For parallel polarization, this mode corresponds to the primitive $\mu=1, \nu=1$ cosine plasmon.

In Fig. 5.4 we also show the energies of $k = 1/R$, $m' = 0$ and $m' = 1$ cylinder plasmons calculated using Eq. (5.30). As one would expect, the infinite cylinder approach provides a perfect description of the torus modes for small aspect ratios. This

is expected since for $X < 0.1$, hybridization is minimal and the two torus modes can be described as pure $\nu=0$ and $\nu=1$ primitive plasmons. However, what is remarkable is that this simple analytical form provides almost perfect agreement with the fully converged hybridized bonding and antibonding torus modes for aspect ratios up to X around 0.9. Although not discussed in detail in this paper, we have also found that the dominant dipole active primitive plasmon modes for perpendicular polarization is a bonding and antibonding hybridized torus mode resulting from the interaction of the $\mu=0$, $\nu=1$ and $\nu=2$ primitive sine plasmon modes. In the cylinder geometry, these primitive plasmons corresponds to cylinder plasmons of wavevector $k=0$ and azimuthal symmetries $m'=1$ and $m'=2$. The energies of the hybridized perpendicular mode agree very well with the corresponding cylinder mode for all aspect ratios. The above observations are significant findings because they enable a very simple modeling of the plasmon resonances of a torus using the analytical approach for an infinite cylinder. Since the inclusion of a realistic dielectric backgrounds is trivial for an infinite cylinder, we will use this analogy in section IV to calculate the sensitivity of the torus plasmon energies to changes in the dielectric background.

5.3.2 Optical absorption

Next, we examine the optical absorption cross sections. First we consider parallel polarization of the incident light. For this geometry only $\mu = 1$ cosine plasmons are relevant. In Fig. 5.5 we show the absorption cross sections for two tori of aspect

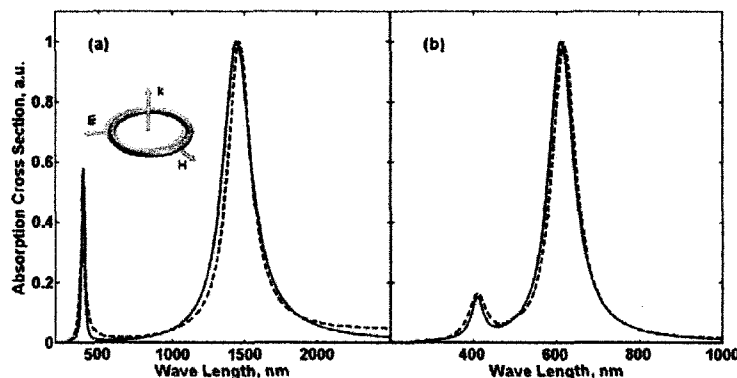


Figure 5.5 Absorption cross sections for light of parallel polarization incident on a torus of aspect ratio $X=0.2$ (a) and $X=0.8$ (b) calculated using PH (red) and FDTD (blue). In the FDTD calculations, the sizes of the tori are $r=2$ nm, $R=10$ nm and $r=2$ nm, $R=2.5$ nm. The damping parameter $\delta=0.2$ eV.

ratios 0.2 and 0.8 along with results from FDTD simulations. The spectra have been normalized to unity peak height. A peak in the absorption spectra appears when ω of the incident wave is in resonance with a hybridized plasmon mode. The intensity of the peak is proportional to the square of its dipole moment,[50] which depends on the relative amplitudes of the primitive plasmons that make up the hybridized state.

The agreement between the results of PH and FDTD is very good. The small differences in the spectra for the small aspect ratio ring is due to FDTD stair-casing errors.[146] For both aspect ratios, the spectra reveals two features. The long wavelength feature is very sensitive to the aspect ratio. This resonance is the hybridized bonding $\nu=0$ mode discussed in Figs. 5.3 and 5.4. The intensity of this feature is large because of the strong admixture of the $\nu=0$ primitive plasmon which has a large dipole moment. The short wavelength resonance does not depend significantly

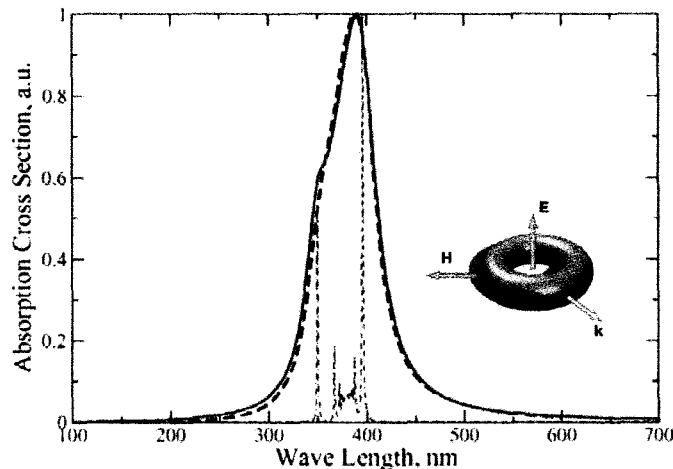


Figure 5.6 Absorption cross sections for perpendicular polarization calculated using PH (red) and FDTD (black) for a torus of $r=5$ nm and $R=10$ nm ($X=0.5$) using a damping of $\delta=0.2$ eV. The dotted green line shows the absorption spectra calculated using a damping $\delta=0.005$ eV.

on aspect ratio and is dominated by the excitation of the hybridized antibonding $\nu=1$ mode. However, several of the higher order hybridized modes depicted in Fig. 5.3 also contribute to the short wavelength absorption feature. Since the energies of these higher energy modes are very close, the individual modes can not be resolved in the spectra. Our calculated spectra agree qualitatively with the results from experiments and other calculations.[141, 143]

In Fig. 5.6, we compare the perpendicular absorption spectra of a torus of aspect ratio $X=0.5$ calculated using PH and FDTD. The agreement is very good also for this polarization. As can be seen in the PH spectrum calculated using an artificially small damping, the absorption feature is made up of several closely spaced optical transitions. Although not discussed in detail in this paper, the calculated hybridized

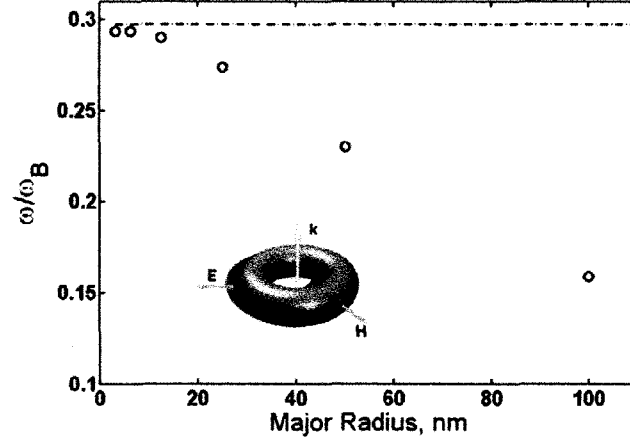


Figure 5.7 Effect of phase retardation on the tunable parallel torus mode. The open circles are the FDTD results for tori of a fixed aspect ratio of $X=0.4$ as a function of the major radius R . The horizontal dotted line shows the PH result.

$\mu=0$ sine plasmon modes are clustered between $\omega/\omega_B=0.65$ and 0.75 in the entire range of aspect ratios, and depend very weakly on X . The two dominant absorption features in Fig. 5.6 are a bonding and antibonding modes formed from the interaction of the primitive $\mu=0$ sine $\nu=1$ and $\nu=2$ modes depicted in Fig. 5.2. As the aspect ratio of the torus increases, the bonding $\nu=1$ mode exhibits a very weak redshift and the antibonding $\nu=2$ mode a very weak blueshift. However, the splitting between the resonances remains too small to be resolved in any calculation performed using a realistic damping parameter δ . As discussed above, these two perpendicular modes can also be well described as infinite cylinder plasmons of energies given by Eq. (5.30) for $k=0$ and $m'=1$ and $m'=2$.

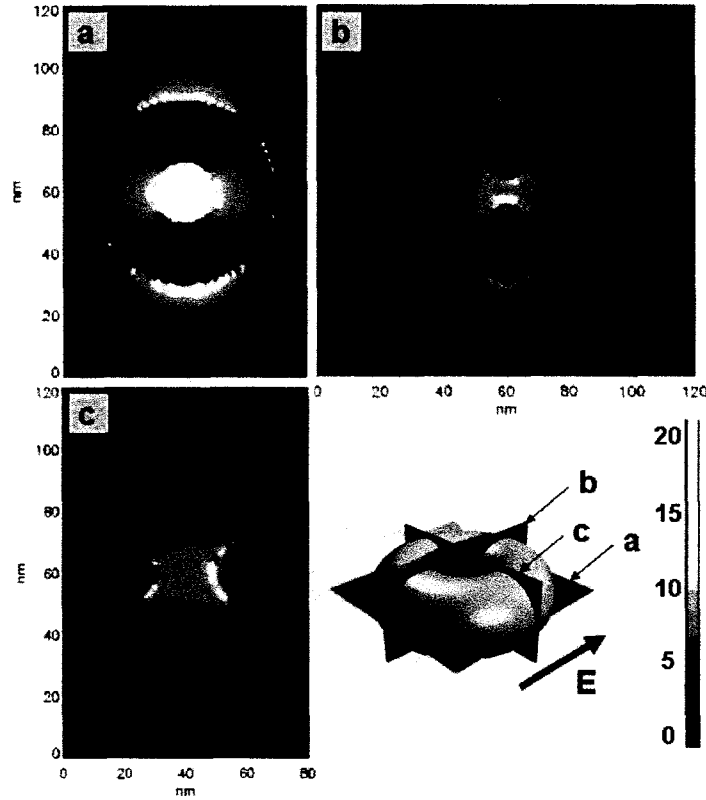


Figure 5.8 Electric field enhancement calculated using FDTD in the three cuts defined by the surfaces (a-c) shown in the inset. The geometry of the torus is $r=10$ nm, $R=20$ nm corresponding to an aspect ratio $X=0.5$. The wavelength of the incident light is 811 nm. The damping is $\delta=0.2$ eV.

5.3.3 Field enhancements and retardation effects

In Fig. 5.7, we investigate the effects of phase retardation on the tunable parallel $\nu=0$ hybridized mode by comparing the PH result with the energies of the lowest energy absorption feature extracted from FDTD spectra for tori of fixed aspect ratios $X=0.4$ but varying radii r and R . As R increases the retardation effects result in the expected redshift of the plasmon resonance relative to the electrostatic PH result.

In Fig. 5.8, we show FDTD calculations of the electric field enhancements for resonant excitation of the low energy dipolar resonance of the torus. The cuts defining the surfaces are shown in the inset. Panel (a) shows that the overall shape of the field enhancement is dipolar as would be expected from the primitive $\mu=1$ $\nu=0$ cosine modes. The largest field enhancements around 50 are induced in the cavity inside the torus. These enhancements are relatively homogeneous as have been pointed out previously.[138] A close inspection of panels (b) and (c) reveals that the field enhancements on the interior surfaces ($\beta = \pm\pi$) are slightly larger than those on the outer surface ($\beta=0$). This asymmetry show that the plasmon mode also contains a $\mu=1$, $\nu=1$ component as expected from the hybridization evidenced in Fig. 5.4. The calculated field enhancements are qualitatively similar and consistent with previously published studies.[142, 141]

5.4 Discussion and Conclusion

Our finding that the tunable parallel dipolar plasmon mode can be well described as an infinite wire plasmon of $m'=0$ and a wavelength equal to the circumference of the torus ($k = 1/R$) makes it easy to calculate the LSPR sensitivities of a metallic torus using realistic dielectric permittivities for the metal. The plasmon frequencies of an infinite metallic wire can be calculated analytically both in the electrostatic and in the fully retarded limit. In the electrostatic limit the parallel dipole resonance is

obtained as the solution of,

$$\frac{\epsilon_R(\omega)}{n_E^2} = \frac{I_0(X)K'_0(X)}{I'_0(X)K_0(X)}, \quad (5.31)$$

where I and K are the modified Bessel functions introduced in Eq. (5.30) and ϵ_R is the real part of the dielectric permittivity of the metal and n_E the refractive index of the surrounding medium. Using experimentally tabulated data for gold,[151] we obtain LSPR sensitivities at $n_E=2.12$ of 444, 861, and 1660 nm/RIU for gold tori of aspect ratios 0.333, 0.2, and 0.909. These values compare very well with the values 444, 880, and 1660 nm/RIU obtained using an alternative analytical approach.[143]

In conclusion, we have extended the Plasmon Hybridization method to a metallic torus. We have shown that the plasmon resonances of a torus result from hybridization of primitive plasmon resonances that can be expressed in terms of toroidal harmonics. For aspect ratios smaller than 0.8, the hybridization is relatively weak and the lowest order dipole active torus plasmon can be described analytically as an infinite cylinder plasmon of a wavelength equal to the circumference of the torus. The calculated optical properties of the torus agree with the results from FDTD simulation and with the results from other theoretical approaches. Our approach can easily be generalized to toroidal shell structures such as a dielectric torus covered by a thin metallic shell. We expect that the plasmon resonances of such a structure will exhibit a similar tunability as other dielectric core-metallic shell structures such as the nanoshell and the nanorice particles.[59]

Chapter 6

Conclusions

Based on plasmon hybridization approach, the optical and plasmonic properties of various metallic nanostructures such as nanoshells, thin films, individual sub-wavelength holes in thin metal film, nanoshell/J-aggregate complexes, and toroidal nanoparticles were clarified. First, using simple and universal concepts we have provided an intuitive explanation for why the seemingly repulsive alignment of the surface charges associated with a bonding nanoshell and thin film plasmon results in plasmon modes of lower energy than the seemingly attractive antisymmetric alignment. We have also demonstrated that the plasmon dispersion for a thin metallic film can be derived from the expression for nanoshell plasmon energies in the limit of a large nanoshell of finite thickness.

After clarifying the nature of plasmon modes of thin metal films, we have presented a simple physical explanation for the experimentally observed resonance in the optical spectra of nanosized holes in thin metallic films. When the hole is present, the film plasmons induce charges on the surfaces of the hole. Film plasmons of certain wavelengths that depend on the diameter of the hole can induce a large dipole moment across the hole. The hole thus mediates a coupling between these specific film plasmons and an incident electromagnetic wave. A simple expression for the wave-

length of the dipole active film plasmons is obtained. For increasing hole diameter, the wavelength of the dipole active film plasmons decreases resulting in a redshifted energy of the hole resonance. Our approach provides a quantitative explanation for the experimentally observed redshift of a hole resonance as a function of hole diameter in previous experiments on films with fixed film thickness. We predict a redshift of the energy of the hole resonance with decreasing film thickness, which is substantiated in experimental measurements on individual nanoholes.

On top of the clarified plasmonic nature of metal nanoshell particles, the hybridization scheme was extended to the coherent coupling between the localized plasmons of a nanoshell and the excitons of J-aggregate molecules adsorbed on the metallic nanoparticle surface. We have shown that the coherent coupling between the plasmons of the nanoshell particle and the excitons of the J-aggregate can create the new hybridized state, using classical electromagnetic theory. The theoretical calculations of optical absorption for nanoshell/J-aggregate complexes could explain the experimental results of the extinction spectra. Strongly asymmetric splitting energies as large as 120 meV are observable in these complexes, where the splitting energy depends upon the plasmon mode of the complex. We believe that this result may stimulate interest in the fabrication and properties of coupled plasmon/exciton nanostructures with controlled coupling, and with optical properties unique to this new class of nanoparticle-based materials.

Finally, the Plasmon Hybridization method was extended to a metallic torus nanoparticle using toroidal coordinates. The plasmon resonances of a torus result from hybridization of primitive plasmon resonances that can be expressed in terms of toroidal harmonics. For aspect ratios smaller than 0.8, the hybridization is relatively weak and the lowest order dipole active torus plasmon can be described analytically as an infinite cylinder plasmon of a wavelength equal to the circumference of the torus. The calculated optical properties of the torus agree with the results from FDTD simulation and with the results from other theoretical approaches.

There are more ways to develop the plasmon hybridization method. For instance in order to describe the plasmon-exciton coupling quantum mechanically for not only nanoparticle/J-aggregate complexes but also nanoparticle/quantum dot conjugated systems, the plasmon hybridization method can be combined to the density matrix formalism.[115] If the quantum mechanical and non-equilibrium effect is considered to the plasmon hybridization method, more interesting optical properties can be studied in the field of nanophotonics combined with nonlinear optics and quantum optics.

References

1. E. Prodan, C. Radloff, N. J. Halas, and P. Nordlander, *Science* **302**, 419 (2003).
2. N. J. Halas, *MRS Bulletin* **30**, 362 (2005).
3. S. Link and M. A. El-Sayed, *J. Phys. Chem. B* **103**, 8410 (1999).
4. C. J. Murphy, T. K. San, C. J. Orendorff, J. X. Gao, L. Gou, S. E. Hunyadi, and T. Li, *J. Phys. Chem. B* **109**, 13857 (2005).
5. S. Lal, S. Link, and N. J. Halas, *Nature Phot.* **1** 641 (2007).
6. Y. Alaverdyan, E.-M. Hempe, A. N. Vamivakas, E. Haibo, S. A. Maier, and M. Atature, *Appl. Phys. Lett.* **94** 021112 (2008).
7. C. Huang, A. Bouhelier, G. C. des Francs, A. Bruyant, A. Guenot, E. Finit, J.-C. Weeber, and A. Dereux, *Phys. Rev. B* **78** 155407 (2008).
8. A. Alu, and N. Engheta, *Phys. Rev. B* **78** 195111 (2008).
9. V. E. Ferry, L. A. Sweatlock, D. Pacifici and H. A. Atwater, *Nano Lett.* **8** 4391-4397 (2008).
10. K. Nakayama, K. Tanabe, and H. A. Atwater, *Appl. Phys. Lett.* **93** 121904 (2008).
11. N. A. Liu, S. Kaiser, and H. Giessen, *Adv. Mat.* **20** 4521–4525 (2008).
12. N. A. Liu, L. Fu, S. Kaiser, H. Schweizer, and H. Giessen, *Adv. Mat.* **20** 3859–3865 (2008).
13. R. J. C. Brown, and M. J. T. Milton, *J. Raman Spectr.* **39** 1313–1326 (2008).
14. M. K. Hossain, Y. Kitahama, G. G. Huang, T. Kaneko, and Y. Ozaki, *Appl. Phys. B* **93** 165–170 (2004).
15. N. G. Khlebtsov, *Quantum Electronics* **38**, 504–529 (2008).
16. E. Prodan, and P. Nordlander, *J. Chem. Phys.* **120**, 5444–5454 (2004).
17. P. Nordlander and E. Prodan, *Nano Lett.* **4**, 2209 (2004).
18. P. Nordlander, C. Oubre, E. Prodan, K. Li, and M. I. Stockman, *Nano Lett.* **4**, 899 (2004).

19. D. W. Brandl, N. A. Mirin, and P. Nordlander, *J. Phys. Chem. B* **110**, 12302 (2006).
20. F. Le, N. Z. Zwin, N. J. Halas, and P. Nordlander, *Phys. Rev. B* **76** 165410 (2007).
21. F. Hao and P. Nordlander, *Appl. Phys. Lett.* **89**, 103101 (2006).
22. H. Raether, *Surface Plasmons on Smooth and Rough Surfaces and on Gratings* (Springer-Verlag, 1988).
23. A. V. Zayats, I. I. Smolyaninov and A. A. Maradudin, *Phys. Rep.* **408** 131-314 (2005).
24. J. A. Dionne, L. A. Sweatlock, H. A. Atwater, and A. Polman, *Phys. Rev. B* **72** 075405 (2005).
25. H. A. Bethe, *Phys. Rev.* **66** 163-182 (1944).
26. C. J. Bouwkamp, *Rep. Prog. Phys.* **17** 35-100 (1954).
27. T. W. Ebbeson, H. J. Lezec, H. F. Ghaemi, T. Thio, and P. A. Wolf, *Nature* **391** 667-669 (1998).
28. J. Zhao, X. Y. Zhang, C. R. Yonzon, A. J. Haes, and R. P. Van Duyne, *Nanomedicine* **1** 219-228 (2006).
29. E. Dulkeith, A. C. Morteau, T. Niedereichholz, T. A. Klar, J. Feldmann, A.A. Levi, F. C. J. M. van Veggel, D. N. Reinhoudt, M. Moller, and D. I. Gittings, *Phys. Rev. Lett.* **89**, 203002 (2002).
30. F. Tam, G. P. Goodrich, B. R. Johnson, and N. J. Halas, *Nano Lett.* **7**, 496 (2007).
31. S. W. Bishnoi, C. J. Rozell, C. S. Levin, M. K. Gheith, B. R. Johnson, D. H. Johnson, and N. J. Halas, *Nano Lett.* **6**, 1687 (2006).
32. A. O. Govorov, and I. Carmeli, *Nano Lett.* **7**, 620-625 (2007).
33. J. Slocik, F. Tam, N. J. Halas, and R. R. Naik, *Nano Lett.* **7**, 1054-1058 (2007).
34. Y. Song, K. Zhao, Y. Jia, X. Hu, and Z. Y. Zhang, *J. Chem. Phys.* **129**, 204506 (2008).

- 35. Y. Alaverdyan, E.-M. Hempe, A. N. Vamivakas, E. Haibo, S. A. Maier, and M. Atature, *Appl. Phys. Lett.* **94**, 021112 (2009).
- 36. M. Fleischer, C. Stanciu, F. Stade, J. Stadler, K. Braun, A. Heeren, M. Haffner, D. Kern, and A. J. Meixner, *Appl. Phys. Lett.* **93**, 111114 (2008).
- 37. T. Rindzevicius, Y. Alaverdyan, B. Sepulveda, T. Pakizeh, M. Kall, R. Hillenbrand, J. Aizpurua, and F. J. G. de Abajo, *J. Phys. Chem. C* **111**, 1207–1212 (2007).
- 38. T. Shegai, Z. P. Li, T. Dadosh, Z. Y. Zhang, and H. X. Xu, *Proc. Natl. Acad. Sci. USA* **105**, 16448–16453 (2008).
- 39. H. X. Xu, *Phys. Rev. B* **72**, 073405 (2005).
- 40. S. J. Kim, and D.-J. Jang, *Mater. Lett.* **62**, 4500–4502 (2008).
- 41. K. Tanabe, *J. Phys. Chem. C* **112**, 15721–15728 (2008).
- 42. L. L. Yang, B. Yan, and B. M. Reinhard, *J. Phys. Chem. C* **112**, 15989–15996 (2008).
- 43. F. Hubenthal, N. Borg, and F. Trager, *Appl. Phys. B* **93**, 39–45 (2008).
- 44. A. O. Pinchuk, and G. C. Schatz, *Appl. Phys. B* **93**, 31–38 (2008).
- 45. D. J. Wu, X. D. Xu, and X. J. Liu, *J. Chem. Phys.* **129**, 074711 (2008).
- 46. A. S. Kirakosyan, and T. V. Shahbazyan, *J. Chem. Phys.* **129**, 034708 (2008).
- 47. D. J. Wu, X. J. Liu, L. L. Liu, and W. P. Qian, *Appl. Phys. A* **92**, 279–282 (2008).
- 48. Y. Hu, R. C. Fleming, and R. A. Drezek, *Opt. Express* **16**, 19579–19591 (2008).
- 49. J. Zhu, *Appl. Phys. Lett.* **92**, 241919 (2008).
- 50. D. W. Brandl and P. Nordlander, *J. Chem. Phys.* **126**, 144708 (2007).
- 51. P. B. Johnson and R. W. Christy, *Phys. Rev. B* **6**, 4370 (1972).
- 52. B. E. Sernelius, *Surface Modes in Physics*, (Wiley-VCH Verlag, Berlin, Germany, 2001).
- 53. J. J. Burke, G. I. Stegeman, and T. Tamir, *Phys. Rev. B* **33**, 5186–5201 (1986).

54. E. N. Economou, *Phys. Rev.* **182**, 539–554 (1969).
55. H. Liu, D. A. Genov, D. M. Wu, Y. M. Liu, Z. W. Liu, C. Sun, S. N. Zhu, and X. Zhang, *Phys. Rev. B* **76**, 073101 (2007).
56. M. Cortie, M. Ford, *Nanotechnology* **18**, 235704 (2007).
57. J. Zhu, *J. Nanosci. Nanotechnol.* **7**, 1059–1064 (2007).
58. P. K. Jain, W. Huang, and M. A. El-Sayed, *Nano Lett.* **7**, 2080–2088 (2007).
59. H. Wang, D. W. Brandl, P. Nordlander, and N. J. Halas, *Acc. Chem. Res.* **40**, 53–62 (2007).
60. G. Guo, N. Liu, L. Fu, T. P. Meyrath, T. Zentgraf, H. Schweizer, and H. Giessen, *Opt. Express* **15**, 12095–12101 (2007).
61. S. Wang, D. F. P. Pile, C. Sun, and X. Zhang, *Nano Lett.* **7**, 1076–1080 (2007).
62. S. A. Maier, P. G. Kik, H. A. Atwater, S.; Meltzer, E.; Harel, B. E. Koel, and A. G. Requicha, *Nature Mat.* **2**, 229–232 (2003).
63. J. R. Krenn, B. Lamprecht, H. Ditlbacher, G. Schider, M. Salerno, and A. Leitner, and F. R. Aussenegg, *Europhys. Lett.* **60**, 663–669 (2002).
64. G. Wei, L. Wang, L. Sun, Y. Song, Y. Sun, C. Guo, T. Yang, and Z. Li, *J. Phys. Chem. C* **111**, 1976–1982 (2007).
65. J. Aizpurua, G. W. Bryant, L. J. Richter, and F. J. G. de Abajo, *Phys. Rev. B* **71**, 235420 (2005).
66. J. Zhang, M. H. Chowdhury, and J. R. Lakowicz, *Nano Lett.* **7**, 2101–2107 (2007).
67. S. Bruzzone, M. Malvaldi, G. P. Arrighini, and C. Guidotti, *Theor. Chem. Acc.* **118**, 67–73 (2007).
68. B. N. Khlebtsov, and N. G. Khlebtsov, *J. Quant. Spectr. Rad. Transf.* **106**, 154–169 (2007).
69. E. M. Larsson, J. Alegret, M. Kall, and D. S. Sutherland, *Nano Lett.* **7**, 1256–1263 (2007).
70. S. Saini, S. Bhowmick, V. B. Shenoy, and B. Bagchi, *J. Photochem. Photobiol. A* **190**, 335–341 (2007).

71. R. S. Swathi, and K. L. Sebastian, *J. Chem. Phys.* **126**, 234701 (2007).
72. M. S. M. Peterson, J. Bouwman, A. Chen, and M. Deutch, *J. Colloid Interface Sci.* **306**, 41–49 (2007).
73. H. I. E. Ahrach, R. Bachelot, A. Vial, G. Lerondel, J. Plain, and P. Royer, *Phys. Rev. Lett.* **98**, 107402 (2007).
74. B.-H. Choi, H.-H. Lee, S. Jin, S. Chun, and S.-H. Kim, *Nanotechnology* **18**, 075706 (2007).
75. P. A. Atanasov, H. Takada, N. N. Nedyalkov, and M. Obara, *Appl. Surf. Sci.* **253**, 8304–8308 (2007).
76. R. L. Chern, X. X. Liu, and C. C. Chang, *Phys. Rev. E* **76**, 016609 (2007).
77. I. Romero, J. Aizpurua, G. W. Bryant, and F. J. G. de Abajo, *Opt. Express* **14**, 9988–9999 (2006).
78. N. Papanikolaou, *Phys. Rev. B* **75**, 235426 (2007).
79. P. K. Jain, and M. A. El-Sayed, *Nano Lett.* **7**, 2854–2858 (2007).
80. F. Kaminski, V.; Sandoghdar, and M. Agio, *J. Comp. Theor. Nanosci.* **4**, 635–643 (2007).
81. S. M. Wang, J. J.; Xiao, and K. W. Yu, *Optics Commun.* **279**, 384–389 (2007).
82. F. J. G. de Abajo, *Rev. Mod. Phys.* **79**, 1267–1290 (2007).
83. J. Henzie, M. H. Lee, and T. W. Odom, *Nature Nanotech.* **2**, 549–554 (2007).
84. H. Gao, J. Henzie, and T. W. Odom, *Nano Lett.* **6**, 2104–2108 (2006).
85. L. Yin, V. K. Vlasko-Vlasov, A. Rydh, J. Pearson, U. Welp, S.-H. Chang, S. K. Gray, G. C. Schatz, D. B. Brown, and C. W. Kimball, *Appl. Phys. Lett.* **85**, 467–469 (2004).
86. D. Korobkin, Y. A. Urzumov, B. Neuner, C. Norman, Z. Zhang, I. D. Mayergoyz, and G. Shvets, *Appl. Phys. A* **88**, 605–609 (2007).
87. G. Gay, O. Alloschery, B. V. de Lesegno, C. O. O'Dwyer, J. Weiner, and H. J. Lezec, *Nature Phys.* **2**, 262–267 (2006).
88. H. J. Lezec, and T. Thio, *Opt. Express* **12**, 3629–3651 (2004).

89. M. W. Kovarz, Appl. Opt. **34**, 3055–3063 (1995).
90. J. Prikulis, P. Hanarp, L. Olofsson, D. S. Sutherland, and M. Kall, Nano Lett. **4**, 1003–1007 (2004).
91. T. Rindzevicius, Y. Alaverdyan, A. Dahlin, F. Hook, D. S.; Sutherland, and M. Kall, Nano Lett. **5**, 2335–2339 (2005).
92. A. Dahlin, M. Zach, T. Rindzevicius, M. Kall, D. S. Sutherland, and F. Hook, J. Am. Chem. Soc. **127**, 5043–5048 (2005).
93. S. H. Chang, S. K. Gray, and G. C. Schatz, Opt. Express **13**, 3150–3165 (2005).
94. K. L. Shuford, S. K. Gray, M. A. Ratner, and G. C. Schatz, Chem. Phys. Lett. **435**, 123–126 (2007).
95. R. Wannemacher, Opt. Comm. **195**, 107–118 (2001).
96. P. Lalanne, J. P. Hugonin, and J. C. Rodier, Phys. Rev. Lett. **95**, 263902 (2005).
97. T. H. Park, N. Mirin, J. B. Lassiter, C. L. Nehl, N. J. Halas, and P. Nordlander, ACS Nano **2**, 25–32 (2008).
98. T. H. Park, and P. Nordlander, Chem. Phys. Lett. **472**, 228–231 (2009).
99. J. Dintinger, S. Klein, F. Bustos, W.L. Barnes, and T. W. Ebbessen, Phys. Rev. B **71**, 035424 (2005).
100. J. Bellessa, C. Bonnard, J. C. Plenet, and J. Mugnier, Phys. Rev. Lett. **93**, 036404 (2004).
101. Y. Sugawara, T. A. Kelf, J. J. Baumberg, M. E. Abdelsalam, and P. N. Bartlett, Phys. Rev. Lett. **97**, 266808 (2006).
102. G. A. Wurtz, P.R. Evans, W. Hendren, R. Atkinson, and W. Dickson, R.J. Pollard, A. V. Zayats, W. Harrison, C. Bower, Nano Lett. **7**, 1297–1303 (2007).
103. G. P. Wiederrecht, G. A. Wurtz, and J. Hranisavljevic, Nano Lett. **4**, 2121–2125 (2004).
104. C. F. Bohren, and D. R. Huffman, *Absorption and scattering of light by small particles* (John Wiley and Sons: New York, 1998).
105. B. K. P. Scaife, *Principles of Dielectrics* (Oxford Science Publications, 1998).

106. P. A. Hobson, W. L. Barnes, D. G. Lidzey, G. A. Gehring, D. M. Whittaker, M. S. Skolnick, and S. Walker, *Appl. Phys. Lett.* **81**, 3519 (2002).
107. J. Song, Y. He, A. V. Nurmikko, J. Tischler, and V. Bulovic, *Phys. Rev. B* **69**, 235330 (2004).
108. D. Lidzey, D. Bradley, M. Skolnick, E. Virgili, and S. Walker, *Phys. Rev. Lett.* **82**, 3316 (1999).
109. D. G. Lidzey, D. D. C. Bradley, A. Armitage, S. Walker, and M. S. Skolnick, *Science* **288**, 1620 (2000).
110. S. J. Oldenburg, R. D. Averitt, S. L. Westcott, and N. J. Halas, *Chem. Phys. Lett.* **288**, 243-247 (1998).
111. P. K. Jain, S. Eustis, and M. A. El-Sayed, *J. Phys. Chem. B* **110**, 18243-18253 (1998).
112. E. Prodan, A. Lee, and P. Nordlander, *Chem. Phys. Lett.* **360**, 325-332 (2002).
113. J. Tempere, I. F. Silvera, and J. T. Devreese, *Surf. Sci. Rep.* **62**, 159 (2007).
114. G. S. Milagre, A. Winder, and A. Moula-Melo, *Phys. Lett. A* **368**, 155 (2007).
115. D. Neuhauser and K. Lopata, *J. Chem. Phys.* **127**, 154715 (2007).
116. H. Hata, Y. Kobayashi, M. Salama, R. Malek, and T. E. Mallouk, *Chem. Mater.* **19**, 6588 (2007).
117. J. C. Garno, C. D. Zangmeister, and J. D. Batteas, *Langmuir* **23**, 7874 (2007).
118. Q. Huo and J. G. Worden, *J. Nanoparticle Res.* **9**, 1013 (2007).
119. R. Sardar and J. S. Shumaker-Parry, *Nano Lett.* **8**, 731 (2008).
120. F. Zhao, J. K. Xun, and S. F. Liu, *Austr. J. Chem.* **61**, 1 (2008).
121. S. Bidault, F. J. G. de Abajo, and A. Polman, *J. Am. Chem. Soc.* **130**, 2750 (2008).
122. K. L. Kelly, E. Coronado, L. L. Zhao, and G. C. Schatz, *J. Phys. Chem. B* **107**, 668 (2003).
123. F. Tam, C. Moran, and N. J. Halas, *J. Phys. Chem. B* **108**, 17290 (2004).

124. G. Pellegrini, G. Mattei, V. Bello, and P. Mazzoldi, *Mat. Sci. Eng. C* **27**, 1347 (2007).
125. J. J. Penninkhof, A. Moroz, A. van Blaaderen, and A. Polman, *J. Phys. Chem. C* **112**, 4146 (2008).
126. V. V. Kulish and P. M. Tomchuk, *Surf. Sci.* **602**, 1045 (2008).
127. D. J. Wu, X. D. Xu, and X. J. Liu, *Solid State Comm.* **146**, 7 (2008).
128. R. D. Averitt, D. Sarkar, and N. J. Halas, *Phys. Rev. Lett.* **78**, 4217 (1997).
129. S. Link, M. B. Mohamed, and M. A. El-Sayed, *J. Phys. Chem. B* **103**, 3073 (1999).
130. M. Ringler, T. A. Klar, A. Schwemer, A. S. Susa, J. Stehr, G. Raschke, S. Funk, M. Borowsky, A. Nichtl, K. Kurzinger, R. T. Phillips, and J. Feldmann, *Nano Lett.* **7**, 2753 (2007).
131. S. A. Maier and H. A. Atwater, *J. Appl. Phys.* **98**, 011101 (2005).
132. K.-Y. Jung, F. L. Texeira, and R. M. Reano, *J. Lightwave Tech.* **25**, 2757 (2007).
133. N. Liu, H. Guo, L. Fu, S. Kaiser, H. Schweizer, and H. Giessen, *Adv. Mater.* **19**, 3628 (2007).
134. L. R. Hirsch, A. M. Gobin, A. R. Lowery, F. Tam, R. A. Drezek, N. Halas, and J. L. West, *Ann. Biomed. Eng.* **34**, 15 (2006).
135. N. J. Florous, K. Saitoh, and M. Koshiha, *IEEE Trans. Nanotechnol.* **6**, 549 (2007).
136. J. Zhang, Y. Fu, M. H. Chowdhury, and J. R. Lakowicz, *J. Phys. Chem. C* **112**, 18 (2008).
137. M. Green and F. M. Liu, *J. Phys. Chem. B* **107**, 13015 (2003).
138. J. Aizpurua, P. Hanarp, D. S. Sutherland, M. Kall, G. W. Bryant, and F. J. G. de Abajo, *Phys. Rev. Lett.* **90**, 057401 (2003).
139. S. I. Bozhevolnyi, E. D. V. S. Volkov, J. Y. Laluet, and T. W. Ebbeson, *Nature* **440**, 508 (2006).
140. F. J. G. de Abajo and J. Aizpurua, *Phys. Rev. B* **56**, 15873 (1997).

- 141. J. Aizpurua, L. Blanco, P. Hanarp, D. S. Sutherland, M. Kall, G. W. Bryant, and F. J. G. de Abajo, *J. Quant. Spectr. Rad. Transf.* **89**, 11 (2004).
- 142. A. Mary, A. Dereux, and T. L. Ferrell, *Phys. Rev.* **B72**, 155426 (2005).
- 143. A. Mary, D. M. Koller, A. Hohenau, J. R. Krenn, A. Bouhelier, and A. Dereux, *Phys. Rev.* **B76**, 2454221 (2007).
- 144. F. Hao, P. Nordlander, M. T. Burnett, and S. A. Maier, *Phys. Rev. B* **76**, 245417 (2007).
- 145. D. Sarkar and N. J. Halas, *Phys. Rev. E* **56**, 1102 (1997).
- 146. C. Oubre and P. Nordlander, *J. Phys. Chem. B* **109**, 10042 (2005).
- 147. S. S. Vinogradov, P. D. Smith, and E. D. Vinogradova, *Canonical problems in scattering and potential theory Part I* (Chapman & Hall/CRC, Boca Raton, Florida, 2000).
- 148. H. Bateman, *Higher Transcendental Functions* (McGraw-Hill, New York, 1953).
- 149. R. W. Scharstein and H. B. Wilson, *Electromagnetics* **25**, 1 (2005).
- 150. S. Segura and A. Gil, *Comp. Phys. Comm.* **124**, 104 (2000).
- 151. E. D. Palik, *Handbook of Optical Constants of Solids* (Academic, San Diego, 1985).